Materials Today Bio 36 (2026) 102677

Contents lists available at ScienceDirect

Materials Today Bio

journal homepage: www.journals.elsevier.com/materials-today-bio

Cascade-driven nanomotor with self-amplifying necrosis targeting and deep tumor penetration for enhanced type I photodynamic immunotherapy

Yuanyuan Yu [a,b,1], Shuhui Chen [a,b,1], Bin Zhao [a,c], Lili Zhao [b], Fang Wang [a,b], Jingwei Xue [a,b,**], Zhongtao Zhang [a,b,*]

[a] Tumor Precise Intervention and Translational Medicine Laboratory, The Affiliated Taian City Central Hospital of Qingdao University, Taian, 271000, China
[b] Shandong Provincial Key Medical and Health Laboratory of Microenvironment Response Biomedical Materials, Taian City Central Hospital, Taian, 271000, China
[c] Department of Natural Medicinal Chemistry, China Pharmaceutical University, Nanjing, 211198, China

ARTICLE INFO

Keywords:
Nitric oxide
Nanomotor
Necrotic target
Deep tumor penetration
Photodynamic immunotherapy

ABSTRACT

Cancer cells adjacent to the necrotic regions within deep-seated tumors exhibit elevated metastatic potential, while photodynamic immunotherapy, which utilizes photosensitizers as triggers to exert synergistic effects of photodynamic therapy (PDT) and anti-tumor immunotherapy, has attracted considerable interest. However, high oxygen dependency and complex biological barriers hinder the efficacy of nanomedicines by restricting reactive oxygen species generation and intratumoral penetration. Herein, a laser-triggered nanomotor (HCAT NPs) with self-amplifying necrosis targeting and deep tumor penetration is prepared for enhanced type I photodynamic immunotherapy. HCAT NPs can accumulate at the tumor site *via* targeting necrotic tissues, while recovered fluorescence emitted from hypericin can be used to self-monitor drug distribution and optimize laser exposure timing. Excitingly, Cu^{2+} significantly enhances type I photosensitivity of hypericin by facilitating electron transfer and glutathione depletion, while cascade reactions triggered by the type I PDT induce the generation of nitric oxide, which synergistically promotes deep tumor penetration with hypericin *via* nanomotor propulsion and remodels vascular networks. Notably, the activated fluorescence emitted from TPE-4NM is utilized to self-report the generation of nitric oxide, while TPE-4NMB can eliminate peroxynitrite, which is related to tumor metastasis. The well-designed HCAT NPs demonstrate potent phototherapy effects against primary breast tumors, recurrences, and distant metastases, providing insight into the development of type I photosensitizers and novel cascade reaction-driven precision strategies for deep tumor ablation.

1. Introduction

Photodynamic therapy (PDT) has emerged as a promising cancer treatment modality due to its high spatiotemporal selectivity, minimal systemic side effects, and non-invasiveness [1,2]. Notably, PDT is increasingly recognized as a robust strategy for systemic cancer management, as it can significantly induce immunogenic cell death (ICD) in tumor cells, increase the local release of damage-associated molecular patterns (DAMPs) and tumor-associated antigens (TAAs), thereby activating anti-tumor immunostimulation [3–8].

However, two major challenges have constrained the therapeutic efficacy of PDT. Firstly, the effective delivery of photosensitizers (PSs) to deep tumors, which are distant from blood vessels, is impeded by high interstitial pressure and solid stress within tumor tissues [9]. Secondly, the highly disordered, tortuous, and excessively-branched intratumoral vasculature results in intratumoral ischemia and hypoxia [10]. This not only directly impairs the intratumoral delivery of PSs but also serves as a pivotal factor in causing necrosis in deep tumor, which subsequently induces tumor immune suppression and poor prognosis [11,12]. Particularly, recent studies have revealed that cancer cells adjacent to these necrotic regions within deep-seated tumors exhibit elevated metastatic potential [13]. These malignant cells can activate

* Corresponding author. Tumor Precise Intervention and Translational Medicine Laboratory, The Affiliated Taian City Central Hospital of Qingdao University, Taian, 271000, China.
** Corresponding author. Tumor Precise Intervention and Translational Medicine Laboratory, The Affiliated Taian City Central Hospital of Qingdao University, Taian, 271000, China.
E-mail addresses: xuejingwei11111@163.com (J. Xue), zhangzhongtao@qdu.edu.cn (Z. Zhang).
[1] Yuanyuan Yu and Shuhui Chen made equal contributions to this work.

https://doi.org/10.1016/j.mtbio.2025.102677
Received 6 October 2025; Received in revised form 18 November 2025; Accepted 12 December 2025
Available online 18 December 2025

hypoxia-induced epithelial-mesenchymal transition (EMT) pathways, thereby rendering this perinecrotic region a critical niche for the acquisition of invasive phenotypes. Consequently, residual tumor cells residing in this microenvironment are highly predisposed to serve as seeds for recurrence and distant metastasis. Unfortunately, the commonly used type II PDT exhibits suboptimal therapeutic performance due to its heavy reliance on oxygen and oxygen consumption during the generation of singlet oxygen ($^1O_2$) *via* energy transfer [14,15].

Therefore, enhancing the intratumoral penetration of PSs and reducing the dependence of PDT on oxygen have emerged as critical strategies to improve its capacity for eradicating residual tumor "seeds".

As early as 2005, the concept that the motion behavior of micro/nanomotors could promote the deep penetration of themselves and loaded drugs in tumor tissues was proposed [16], and was gradually validated at the two-dimensional planar cellular level [17], three-dimensional multicellular spheroid level [18], and *in vivo* level [19,20]. The validation of this concept provides new insights into overcoming the challenge of poor drug penetration in tumor tissues for conventional nano-drug delivery systems, particularly for therapies directly targeting cancer cells, such as chemotherapy, photothermal therapy, and PDT [9]. Notably, recent studies confirm that nanomotor motility not only improves penetration of the motors and co-delivered therapeutics but also enhances deep T-cell infiltration, offering new strategies to amplify PDT-mediated immune activation [17,19].

Nevertheless, significant challenges remain in utilizing substrate-driven self-chemotaxis of motors for targeted accumulation. Although concentration gradients of substrates may exist between peripheral environments and target sites, nanomotors frequently lose their chemotactic capacity due to premature depletion of "fuel" during migration [21]. Moreover, most reported nanomotors exhibit stochastic motion without directional control mechanisms to guide them toward deep tumor strata [18–20,22]. Consequently, substantial mechanical energy is dissipated as non-productive work, severely compromising their penetration efficacy in solid tumors.

In fact, necrotic tissues within deep tumor strata serve as intrinsic targeting guides for deep-seated regions and enable nanomotors to selectively eliminate recurrence/metastasis seeds in perinecrotic niches [13]. For instance, the clinically used radiopharmaceutical ^{131}I-chTNT, which targets intratumoral necrosis, has demonstrated remarkable efficacy in the precise diagnosis and treatment of lung cancer, hepatocellular carcinoma, and other malignancies. Critically, the light-activatable property of PDT provides a spatiotemporally controllable trigger to regulate nanomotor motility on demand [23].

Mechanistically, reactive oxygen species (ROS) serve as the primary therapeutic agents in PDT, mediating both direct tumor cytotoxicity and antitumor immunity. Based on their ROS generation mechanisms, PDT can be classified into type I and type II pathways [14,15]. Type II PSs (PSs) produce singlet oxygen ($^1O_2$) through triplet energy transfer to molecular oxygen—a process critically dependent on ambient oxygen concentrations, resulting in diminished efficacy under hypoxia. In contrast, type I PSs generate radicals (*e.g.,* superoxide anion ($O_2^{\cdot-}$), hydrogen peroxide (H_2O_2), hydroxyl radical (·OH)) *via* electron transfer with substrates or oxygen, exhibiting superior hypoxia tolerance due to minimal oxygen dependence. However, most reported porphyrin- and phthalocyanine-based PSs remain type II agents, significantly limiting PDT's applicability in hypoxic tumors [24,25]. To date, diverse type I PSs, including metal-organic framework nanomaterials [26], metal oxides [27], carbon-based nanomaterials [28], and organic molecules [29–32], have emerged as effective hypoxia-resistant cancer therapies. Nevertheless, complex synthesis, high production costs, and insufficient structure-activity understanding impede their translational progress [5]. In fact, rational enhancement of type I behavior in existing type II PSs represents a promising alternative strategy. For instance, a recent study reported that thymoquinone, acting as an electron transfer mediator, can convert type II PSs to type I ones, offering novel design principles for PSs modification [33].

Beyond augmenting reactive oxygen species (ROS) generation efficiency, disrupting intratumoral redox homeostasis represents a promising strategy to potentiate PDT. This is because elevated glutathione (GSH) levels in tumor cells can scavenge PDT-generated ROS, directly compromising therapeutic efficacy. Although metal ions [34–36] (*e.g.,* Cu^{2+}, Pt (IV)) and natural products [37,38] (*e.g.,* curcumin, gambogic acid) can amplify oxidative damage by inhibiting GSH biosynthesis or depleting cellular GSH pools—thereby promoting tumor cell apoptosis and ICD—this approach remains nascent. In particular, how to effectively integrate GSH depletion strategies with PDT remains an outstanding challenge in the field.

Herein, we report an intelligent nitric oxide (NO)-driven nanomotor that orchestrates deep tumor penetration, self-monitored NO release, and metastasis-suppressed immunotherapy through a 'necrosis-targeting to necrosis-inducing' self-amplifying cycle. The self-assembled theranostic nanomotor (HCAT) comprises hypericin (HPC), copper (II) ions (Cu^{2+}), L-arginine (L-Arg), and aggregation-induced emission (AIE) fluorogen TPE-4NMB (Scheme 1a). Specifically, HPC serves as both a photosensitizer and necrotropic guidance module, directing deep tumor penetration. Cu^{2+} not only depletes GSH in tumor cells, indirectly enhancing HPC-mediated PDT, but also acts as an electron transfer mediator to directly improve the type I photosensitizing performance of HPC, reducing its dependence on oxygen. L-Arg functions as a substrate for NO generation in the cascade reaction mediated by type I photosensitization, promoting the motion of the nanomotor toward deep tumor regions while remodeling the tumor vascular network to alleviate hypoxia. TPE-4NMB enables real-time NO generation monitoring and scavenges peroxynitrite ($ONOO^-$) generated in the cascade reaction, minimizing $ONOO^-$-mediated adverse tumor prognoses. Through this precise design, a positive feedback loop between the enhanced PDT and necrosis-targeting is achieved, thereby suppressing both primary tumors and distant metastases (Scheme 1b). This study will provide new insights into the development of type I PSs and offer a novel strategy for cascade reaction-driven precision diagnostics and therapeutics in breast cancer.

2. Materials and methods

2.1. Preparation and characterization of HCAT

HCAT, HCA, HAT and HCT nanoparticles were all prepared *via* the one-step nanoprecipitation method. Briefly, the HCAT was prepared as follows: HPC (4 mg), $CuCl_2$ (2 mg), TPE-4NMB (1 mg, Fig. S1) and DSPE-PEG_{2000} (3 mg, Fig. S1) were co-dissolved in dimethyl sulfoxide (DMSO, 500 μL) and then added dropwise into water (9.5 mL) containing L-Arg (2 mg) under intense stirring. Next, the solution was dialyzed against water for 24 h to remove the organic solvent. HCA, HAT and HCT NPs were prepared with a similar procedure, except that TPE-4NMB, $CuCl_2$, L-Arg was not added, respectively. The drug loading of HPC, Cu^{2+}, and L-Arg in HCAT was detected by a fluorescence spectrophotometer at 605 nm, ICP-MS, and Elisa kit, respectively.

The size and *zeta* potential were obtained by ZETASIZER PRO (Malvern Instruments, U.K.). Transmission electron microscopy (TEM, HT7700, Hitachi) was used to characterize the nanoparticles' morphology. UV–Vis absorption and fluorescence spectra were recorded on a Thermo Scientific VARIOSKAN LUX spectrophotometer.

2.2. Self-monitoring the generation of NO by HCAT

Griess Reagent was used to detect the generation of NO, and the procedure was performed following the instructions provided by the supplier. Moreover, the UV–Vis absorption and fluorescence spectra of HCAT before and after irradiation were recorded by a Thermo Scientific VARIOSKAN LUX spectrophotometer. DAF-FM DA (5 μ_M) was used as a probe to visualize intracellular NO. 4T1 cells were seeded into confocal

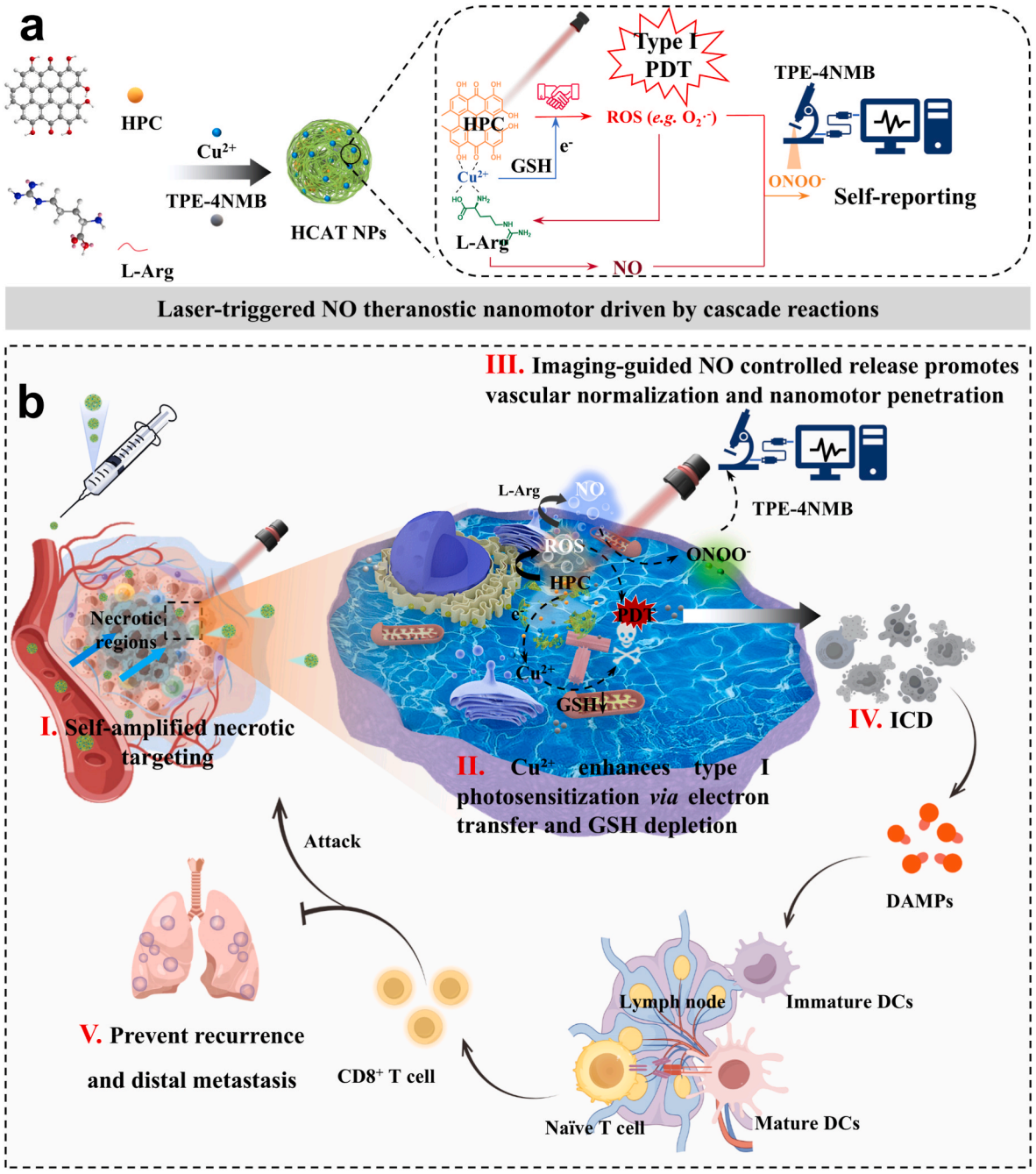

Scheme 1. Schematic illustration of the (a) preparation of HCAT nanomotor, and the principles of cascade reactions triggered by enhanced type I PDT. b) The applications of HCAT NPs in self-amplifying necrosis targeting and deep tumor penetration for enhanced type I photodynamic immunotherapy.

dishes at a density of 2×10^4 per well and allowed to adhere overnight. Then, they were treated with the free HPC (20 μg mL^{-1}), HCT (HPC = 20 μg mL^{-1}), and HCAT (HPC = 20 μg mL^{-1}) for 4 h, followed by washing with cold PBS, and then incubated for another 12 h before being treated with DAF-FM DA and irradiated with a 638 nm laser for 1 min. Confocal laser scanning microscope (CLSM) was used to capture images. (TPE-4NM: λex/em = 405 nm/480–600 nm; DAF-FM: λex/em = 488 nm/510–550 nm)

2.3. Analysis of $ONOO^-$ elimination

BBoxiProbe@O56 was used as the probe for monitoring the residual $ONOO^-$ in cells [39]. 4T1 cells were seeded into confocal dishes at a density of 2×10^4 per well. After 24 h of adherence, the cells were cultured in medium containing HCA (HPC = 20 μg mL^{-1}) or HCAT (HPC = 20 μg mL^{-1}) for 4 h. Then, they were washed with cold PBS and incubated for another 12 h before treatment with BBoxiProbe@O56 (1:1000) and irradiation with a 638 nm laser for 1 min. Finally, CLSM was used for imaging (BBoxiProbe@O56: λex/em = 488/510–550 nm).

2.4. Depletion of GSH by Cu^{2+}

Reduced glutathione (GSH, 100 μ_M) was co-incubated with various formulations for 10 min, and then the residual concentration of GSH was measured using a GSH assay kit according to the manufacturer's instructions. Saline was used as the control.

2.5. Necrosis-targeting evaluation In vitro

Multicellular tumor spheroid (MTSs) composed of 4T1 cells were constructed according to the literature [40]. After culturing the MTSs for three days, uniform ones were chosen to evaluate the distribution of necrotic cells. Specifically, calcein AM (2 μ_M) and PI (8 μ_M) staining solutions were prepared and cocultured with MTSs for 20 min, while the co-localization of HPC (1 μg mL^{-1}) in the spheroids was observed using CLSM after co-incubation with MTSs for 24 h.

2.6. Penetration of multicellular tumor spheroid

Briefly, the spheroids were treated with various samples (HPC, HAT, HCT, HCA, HCAT, ZnPc-CAT) at a concentration of 20 μg mL^{-1} for 4 h, and then irradiated with a 638 nm laser (0.5 W cm^{-2}) for 1 min or not, followed by incubation for 2 h. Subsequently, the culture medium was removed, and the tumor MTSs were washed carefully with cold PBS twice and observed *via* CLSM with Z-stack scanning (Carl Zeiss LSM 900, Germany). λex/em = 561/580−700 nm.

2.7. Immunogenic cell death induction of HCAT In vitro

Immunofluorescence was employed to detect the distribution of CRT and intracellular HMGB1. Briefly, 4T1 cells were seeded at a density of 2 × 10^4 cells per well for 12 h and then treated with different samples (HPC = 20 μg mL^{-1}) for 4 h before the irradiated groups were exposed to a 638 nm laser (0.5 W cm^{-2}) for 1 min. Subsequently, the cells were further cultured for 4 h before being incubated with anti-CRT antibodies or permeabilized with 0.1 % Triton X-100, and incubated with an anti-HMGB1 primary antibody and a FITC-conjugated monoclonal secondary antibody. Nuclei were counterstained with DAPI and imaged by the CLSM. DAPI: λex/em = 405/400−600 nm; FITC: λex/em = 488/500−700 nm.

For ATP secretion detection, 4T1 cells were seeded in a 24-well plate (5 × 10^4 cells per well) for 12 h, treated with samples (20 μg mL^{-1}) for 4 h, and irradiated as before. Then the supernatant was collected after 4 h, and ATP levels were measured using a commercial kit according to the manufacturer's instructions.

2.8. Evaluation of tumor antigen presentation ability of BMDCs In vitro

Bone marrow-derived dendritic cells (BMDCs) were obtained from Balb/c mice and cultured in RPMI 1640 with 10 % FBS, 20 ng mL^{-1} murine GM-CSF and 20 ng mL^{-1} IL-4. Medium was refreshed on day 3, and non-adherent cells were collected after 4 more days. 4T1 cells were pre-treated with various samples for 24 h, and then co-cultured with immature DC cells (1 × 10^6 cells per well) for 24 h. Then, DC cells were stained with live/dead, anti-CD45-APC/Fire 810, anti-CD11c-Brilliant Violet 421 and anti-IA/IE-FITC antibodies, and their tumor antigen presentation ability were assessed *via* flow cytometry.

2.9. Self-reporting of drug distribution and NO generation In Vivo

To further investigate the distribution and metabolism of the prepared HCAT, 4T1 tumor-bearing mice were intravenously administered with HCAT (HPC = 2 mg kg^{-1}, 100 μL) *via* tail vein. Then, the mice were imaged *via* a Tanon *in vivo* imaging system (ABL X6, Shanghai, China) at different time points postinjection (2, 6, 12, 24, and 48 h, respectively). Subsequently, the major organs (heart, liver, spleen, lung, and kidney) and tumors were collected and imaged by IVIS. (λex/em = 365/420−700 nm).

To monitor real-time *in vivo* NO generation during treatment, HCAT (2 mg kg^{-1} of free HPC equivalent, 100 μL) was injected into the tail vein of 4T1-bearing mice. After 12 h postinjection, DAF-FM DA (5 μ_M) was used as a commercial probe of NO *via* intratumoral injection. Then, irradiation was conducted with a 638 nm laser (0.5W cm^{-2}) for 10 min, and images were acquired at 12 h, and 24 h post-irradiation. Mice without irradiation were used as controls. Subsequently, the mice were euthanized, and the tumors were collected and imaged at 24 h post-irradiation. (TPE-4NM: λex/em = 430 nm/500 nm; DAF-FM: λex/em = 500 nm/520 nm).

2.10. Necrotic targeting and deep tumor penetration In Vivo

To demonstrate HPC's impact on enhancing nanoparticle accumulation in tumors, necrotic zones and nanoparticle distributions were examined using H&E staining and IVIS. Moreover, HPC in HCAT was substituted with the traditional photosensitizer ZnPc. ZnPc-CAT (ZnPc = 2 mg kg^{-1}, 100 μL) was administered intravenously to 4T1-bearing mice. After 24 h, mice were sacrificed, and tumors were imaged using a Tanon *in vivo* imaging system (ABL X6, Shanghai, China). In addition, paclitaxel (PTX, 2 mg kg^{-1}, 60 μL) was administered *via* intratumoral injection to aggravate tumor necrosis. After 24 h, ZnPc-CAT (ZnPc = 2 mg kg^{-1}, 100 μL) or HCAT were administered *via* the tail vein. Then, the mice were sacrificed, and the tumors were imaged using the IVIS system. Furthermore, tumor slices from various groups at the same depths were imaged by CLSM and a slice scanner. (λex/em = 561 nm/580−700 nm)

2.11. In Vivo antitumor therapy

The 4T1 tumor-bearing mice with a tumor volume of 80 mm^3 were randomly divided into seven groups (10 mice in each group) including PBS, HCAT without laser (HCAT (−), HPC = 2 mg kg^{-1}, 100 μL), HCAT with laser (HCAT (+), HPC = 2 mg kg^{-1}, 100 μL), HAT with laser (HAT (+), HPC = 2 mg kg^{-1}, 100 μL), HCT with laser (HCT (+), HPC = 2 mg kg^{-1}, 100 μL), HCA with laser (HCA (+), HPC = 2 mg kg^{-1}, 100 μL), HPC with laser (HPC (+), 2 mg kg^{-1}, 100 μL). Mice received tail vein injections every other day. Irradiation was performed 6 h post-injection and lasted for 5 min. The tumor volume and body weight of mice in each group were recorded every other day for 14 days, and the tumor volume was calculated as follows:

$$\text{Volume} = \text{Length} \times \text{Width}^2/2 \ (n = 10)$$

On day 14, the mice were sacrificed, and their tumors were collected, fixed, embedded in paraffin, and sectioned for hematoxylin and eosin (H&E) staining. Subsequently, tumor cell apoptosis was analyzed by immunofluorescence staining using TdT-mediated dUTP nick-end labeling (TUNEL). The expression of CD31, HIF-1α, Ki67, 3-NT, MMP-9, TGF-β, E-cadherin, and vimentin was detected by immunohistochemistry staining.

2.12. ICD effect evaluated In Vivo

To determine the *in vivo* ICD effect, CRT exposure and HMGB1 release were assessed. Briefly, mice with 4T1 breast cancer were treated with different formulations. On day 14, tumor sections were stained with anti-CRT and anti-HMGB1 antibodies, followed by incubation with secondary antibodies to analyze CRT and HMGB1 expression.

2.13. Tumor antigen presentation ability evaluation In Vivo

The expression of major histocompatibility complex class II was measured to evaluate tumor antigen presentation ability of mature DCs. The draining lymph nodes were homogenized to prepare a single-cell suspension, which was then stained with live/dead, anti-CD11b-Brilliant Violet 605, anti-CD11c-Brilliant Violet 421, and anti-IA/IE-FITC antibodies for 30 min at 4 °C in the dark. After washing, the cells were resuspended in staining buffer for flow cytometry analysis.

2.14. Tumor infiltrating lymphocytes analysis

Tumors were sectioned into smaller fragments, then immunofluorescence and flow cytometry were used to evaluate the infiltration of $CD8^+$ T cells. Briefly, the tumor sections were stained with anti-CD8 antibodies to visualize $CD8^+$ T cells. For flow cytometry analysis, tumors were digested with 1 mg mL^{-1} collagenase IV and collected *via* centrifugation. Then anti-CD3-Alexa Fluor 532, anti-CD4-PerCP-Cyanine5.5, anti-CD8a-Brilliant Violet 650, and anti-CD25-PE antibodies were incubated with the suspensions to analyze cytotoxic T lymphocytes ($CD3^+CD8^+$) and Tregs ($CD3^+CD4^+CD25^+$). To analyze tumor-associated MDSCs, the tumor single-cell suspensions were also stained with anti-CD11b-Brilliant Violet 605, anti-Ly6C-APC/Cyanine7 and anti-Ly6G-Brilliant Violet 510. To analyze NK cells, the suspensions were stained with anti-CD45-APC/Fire 810, anti-CD49b-APC and anti-CD3-Alexa Fluor 532.

2.15. Effect of anti-tumor recurrence and immune response analysis of anti-tumor recurrence

In this study, a recurrent tumor model was developed to evaluate the efficacy of immunotherapy. Initially, 4T1-Luc cells (1×10^6) were implanted into the left mammary gland of each female Balb/c mouse. Once the tumor volume reached 100 mm^3, the mice were randomly assigned to different groups. On days 1, 3, and 5, the mice received intravenous injections of 100 μL of either saline, free HPC, HAT, HCT, HCA, or HCAT, all administered at a consistent HPC dose of 2 mg kg^{-1}. The laser treatment groups were exposed to a 638 nm laser for 5 min. Every seven days, the mice were intraperitoneally injected with 15 mg kg^{-1} D-luciferin (200 μL) to facilitate tumor volume imaging *via* bioluminescence intensity. Two days following the final injection, the mice underwent mammary gland lumpectomy. On day 14, 4T1-Luc cells (5×10^5) were implanted into the right mammary gland of each mouse, and the volume of the recurrent tumor was measured every two days. At day 28, the lymphocytes in recurrent tumors and spleens were collected to conduct the flow cytometry detection, and the analyze procedure was similar to that in tumor infiltrating lymphocyte analysis.

2.16. Statistical analysis

Data analysis was performed using GraphPad Prism 8.0.2 software to calculate mean ± standard deviation (SD). Student's t-test was used to assess significant differences between two groups, while One-way or Two-way ANOVA was used to assess significant differences when compared with more than two groups, while $^*p < 0.05$, $^{**}p < 0.01$, $^{***}p < 0.001$, $^{****}p < 0.0001$ indicating significance, and ns indicating no significance.

3. Results and discussion

3.1. Preparation and characterization of HCAT NPs

In recent years, carrier-free nanomedicines—formed through spontaneous co-assembly of natural products leveraging their intrinsic structural properties—have emerged as promising platforms for ultra-high drug loading [41,42]. These systems synergize bioactive natural compounds with nanomaterial functionalities, demonstrating broad utility in drug delivery, bioimaging, and antimicrobial applications.

Hypericin (HPC), a naturally derived photosensitizer, has been validated to exhibit dual type I/II photodynamic activity [43,44]. However, its extensive conjugated system results in poor aqueous solubility, limiting biomedical application. In this study, we have employed HPC as the core therapeutic agent and successfully fabricated HCAT nanoparticles (NPs) (Fig. 1a) through co-assembly with Cu^{2+}, L-arginine (L-Arg), and TPE-4NMB (Fig. S1) *via* a nanoprecipitation method. A distinct Tyndall effect was observed for HCAT NPs under laser irradiation (Fig. 1b), confirming their colloidal behavior in aqueous solution and indicating successful self-assembly.

Ultraviolet–visible (UV–Vis) absorption spectroscopy (Fig. 1c) revealed that HCAT NPs retained the characteristic absorption peaks of HPC at 400–500 nm and 500–600 nm. However, detailed comparative analysis demonstrated significantly reduced UV absorption for HCAT compared to an equivalent mass of HPC within the 350–500 nm range. Notably, the sharp dual absorption peaks of HPC at 550–650 nm were broadened into a single redshifted peak ($\lambda_{max} = \sim 600$ nm), while the absorption band near 380 nm was also markedly attenuated in HCAT NPs. These spectral modifications suggest intermolecular interactions between HPC and other components within HCAT NPs during self-assembly. These spectral shifts suggest intermolecular interactions during co-assembly, further supported by fluorescence quenching at 550–800 nm (Fig. 1d).

The formation of spherical HCAT NPs was confirmed by transmission electron microscopy (TEM, Fig. 1e) and dynamic light scattering (DLS, Fig. 1f). DLS analysis indicated a hydrodynamic diameter of 174.9 nm and a polydispersity index (PDI) of 0.170, suggesting uniform particle size distribution. The size approaching 200 nm facilitates tumor accumulation through the enhanced permeability and retention (EPR), while the colloidal stability was ensured by a measured *zeta* potential of −12.8 mV (Fig. 1g). Quantitative fluorescence spectrophotometry determined the HPC drug loading capacity in HCAT NPs to be 52.2 %, while the drug loading of Cu^{2+}, L-Arg, and TPE-4NMB in HCAT NPs was 22.25 %, 7.88 % and 7.65 %, respectively, surpassing conventional nanomedicines in loading efficiency and significantly reducing the required therapeutic dose. Other NPs (HAT, HCT, HCA) were prepared following similar procedures, while their hydrodynamic diameters were determined as 131.1 nm, 146.6 nm, and 119.0 nm, respectively. Notably, the PDI of HCA was as high as 0.441, indicating a broad size distribution and suggesting potential structural instability (Fig. S2). This was corroborated by its inferior storage stability and faster drug release compared to HCAT NPs (Fig. S3), underscoring the critical role of TPE-4NMB in enhancing the structural stability of HCAT NPs.

Molecular dynamics (MD) simulations elucidated the temporal self-assembly behavior of HCAT. In aqueous-phase simulations (Fig. 1h), adjacent molecules formed clusters at 20 ns, followed by progressive incorporation of free molecules and internal structural optimization. The spherical structure observed in the MD simulations aligns with the results obtained from TEM (Fig. 1e). Structural stability was confirmed by root-mean-square deviation (RMSD) and radius of gyration (Rg) analyses. Notably, in the 80 ns snapshot, the cluster was observed moving to the bottom of the simulation box and subsequently crossing to the top (Fig. 1h), which accounts for the fluctuations in RMSD and Rg between 70 and 80 ns (Fig. 1i and j). Subsequently, RMSD fluctuations progressively diminished after 85 ns, stabilizing within ±0.1 nm (Fig. 1i), while Rg analysis demonstrated convergence near 2.3 nm (Fig. 1j), indicating structural equilibration around 85 ns. The solvent-accessible surface area (SASA) exhibited a continuous decline, converging to approximately 220 nm^2 by the end of the simulation (Fig. 1k).

3.2. Self-assembly mechanism of HCAT NPs

MD simulation, the introduction of force inhibitors, and spectral characterization were utilized to investigate the possible formation mechanisms of HCAT NPs. MD simulation results showed that coordination bond, hydrophobic interaction and hydrogen bond were the main driving forces to promote the formation of HCAT NPs (Fig. 2a).

To evaluate the intermolecular forces in the prepared HCAT NPs, NaCl, urea, sodium hydroxide (NaOH), sodium dodecyl sulfate (SDS), and ethylenediaminetetraacetic acid (EDTA) were used to disrupt electronic forces, hydrogen bonds, hydrophobic interactions, and coordination bonds, respectively (Fig. 2b) [45,46]. As depicted in Fig. 2c, the introduction of SDS, EDTA, urea, and NaOH have induced the nanoparticle decomposition or aggregation, evidenced by increased

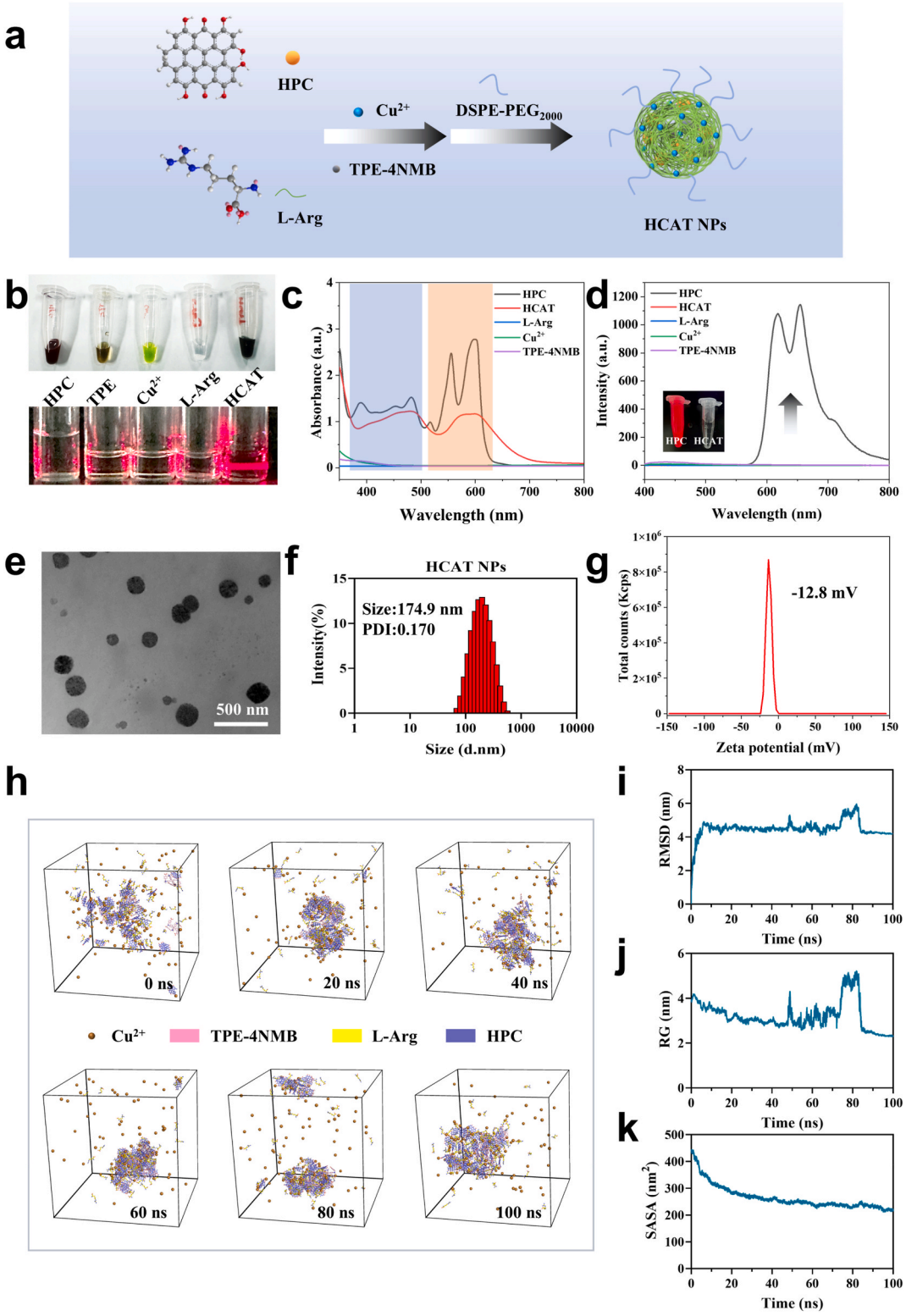

Fig. 1. Preparation and characterization of HCAT NPs. a) Schematic illustration of the preparation of HCAT NPs. b) Appearance photos and Tyndall effect of various formations. c) UV–Vis and (d) fluorescence spectra of HPC, L-Arg, $CuCl_2$, TPE-4NMB, and HCAT NPs (the excitation wavelength was 365 nm). e) TEM images, f) hydrodynamic diameter distributions and g) *zeta* potential of HCAT NPs. h) Molecular cluster changes of HPC, L-Arg, Cu^{2+}, and TPE-4NMB during 100 ns simulation (blue: HPC; yellow: L-Arg; brown: Cu^{2+}; pink: TPE-4NMB). i) Variation of RMSD, j) RG, and k) SASA with simulation time. (For interpretation of the references to color in this figure legend, the reader is referred to the Web version of this article.)

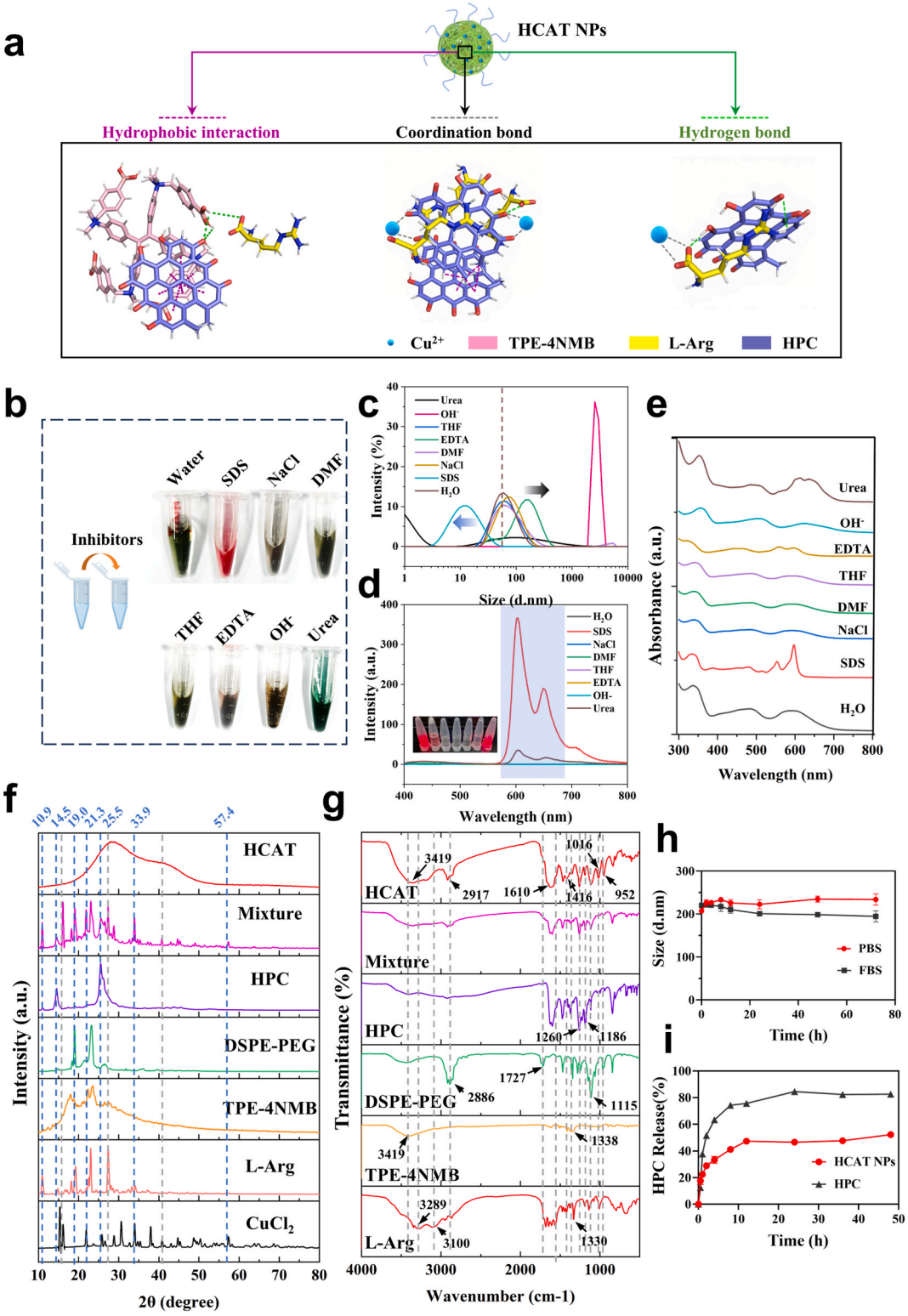

Fig. 2. Assembly mechanism of HCAT NPs. a) Intermolecular interactions analysis in the HCAT NPs. b) Appearance and c) size changes of HCAT after co-incubated with different inhibitors. d) Fluorescence and e) UV–Vis spectra changes of HCAT after co-incubated with different inhibitors. f) XRD, and g) FTIR spectra of various formations. h) Size changes of HCAT NPs in different media at 37 °C over 72 h. i) Cumulative HPC release from free HPC or HCAT NPs over 48 h.

hydrodynamic diameters or broadened size distributions, while NaCl, tetrahydrofuran (THF), dimethylacetamide (DMF) showed negligible effects on particle size or PDI (Fig. 2c). UV–Vis spectral analysis revealed significant alterations in SDS-, EDTA-, urea-, and NaOH-treated groups: where the absorption peaks of HPC at 554 nm and 596 nm exhibited a red shift or enhanced intensity (Fig. 2d). Moreover, the self-quenched fluorescence at 605 nm and 651 nm of HCAT NPs was recovered after the solution was added into SDS or urea (Fig. 2e), indicating that the HCAT NPs would disassemble in the presence of SDS, EDTA, urea and NaOH, suggesting hydrophobic effects, coordination interaction and

hydrogen bonds are the primary driving forces to promote HCATs self-assembly.

Thermogravimetric analysis (TGA) was employed to investigate the thermal stability and compositional attributes of HCAT NPs (Fig. S4), HCAT exhibited a distinct two-stage decomposition profile compared to individual components and their physical mixture. An elevated initial decomposition temperature (134.29 °C) was observed, followed by secondary decomposition at 347.94 °C. This atypical behavior suggests modified intermolecular interactions and molecular packing within HCAT, yielding enhanced thermodynamic stability.

X-ray diffraction (XRD) analysis elucidated crystalline properties (Fig. 2f). $CuCl_2$, L-Arg, TPE-4NMB, DSPE-PEG, and HPC displayed sharp diffraction peaks between 10° and 40°, confirming crystalline structures. The physical mixture retained characteristic peaks at 10.9°, 14.5°, 19.0°, 21.3°, 25.5°, 33.9°, and 57.4° with high resolution, indicating preserved crystallinity without structural reorganization. Conversely, HCAT NPs exhibited substantial structural alterations: peaks at 10.9°, 14.5°, and 19.0° disappeared, while remaining peaks broadened with reduced intensity. A novel broaden peak emerged near 40°, indicating reduced crystallinity, increased amorphous content, and nucleation of a new crystalline phase during molecular packing rearrangement. This contrast highlights structural evolution distinct from physical mixtures, emphasizing synthesis-dependent modulation of crystallinity and phase behavior, which may influence solubility, dissolution, bioavailability, and physicochemical properties.

Fourier-transform infrared (FTIR) spectroscopy revealed molecular vibration changes (Fig. 2g). HCAT NPs exhibited a broad O-H stretching band near 3400 cm^{-1} with significantly enhanced intensity *versus* the physical mixture or HPC group, characteristic of hydrogen-bonded hydroxyl groups. Carbonyl stretching vibrations (1640-1590 cm^{-1}) from HPC quinoid rings showed slight broadening, which can be attributed to the hydrogen-bonding interactions. Notably, HCAT displayed pronounced signals at 1016 cm^{-1} and 952 cm^{-1} absent in the mixture, potentially attributable to: 1) crystal phase transformation unmasking fingerprint vibrations of L-arginine/DSPE-PEG_{2000}, or 2) new Cu-O bonds from Cu^{2+} coordination with HPC phenolic hydroxyls. Additionally, the C-H stretching vibration of phospholipid chains in DSPE-PEG_{2000} was confirmed by the signal at 2886 cm^{-1}, while the strong C-O-C stretching band at 1115 cm^{-1} validated successful integration of PEG chains, indicating effective nano-stabilization.

^1H NMR analysis further corroborated structural changes (Fig. S5). Notably, most proton signals were attenuated or disappeared entirely, particularly the aromatic proton signals (δ 6.50–8.0 ppm) from HPC and TPE-4NMB. This phenomenon suggests that hydrophobic interactions during self-assembly may shield these aromatic protons, rendering them undetectable. Further observation revealed a distinct downfield shift of the HPC methyl group (-CH_3) signal from δ 2.73 ppm to δ 2.86 ppm. This shift likely arises from reduced electron cloud density around the methyl protons due to intermolecular hydrophobic interactions. Similarly, the -OCH_2- signal of DSPE-PEG at δ 3.50 ppm exhibited a downfield shift, indicating that the PEG chains engage in non-covalent interactions with adjacent molecules rather than existing as physically entrapped components. Detailed analysis showed that near-complete attenuation of L-Arg proton signals at δ 3.0–3.2 ppm and δ 1.57 ppm. This absence strongly suggests that L-Arg is encapsulated within the core of nanoparticle rather than adsorbed on the surface or loosely associated with the periphery.

Collectively, these spectroscopic observations confirm the successful fabrication of HCAT NPs. The self-assembly process appears to be driven by a synergistic interplay of intermolecular forces, including hydrogen bonding, hydrophobic interactions, and coordinate covalent bonding. The structural reorganization during nanoparticle formation leads to unique supramolecular architectures with distinct physicochemical properties compared to physical mixtures or individual components.

Stability studies (Fig. 2h) demonstrated minimal particle size fluctuation and sustained PDI values < 0.2 over 72 h in phosphate-buffered saline (PBS, pH 7.4) and fetal bovine serum (FBS), confirming robust colloidal stability and structural integrity for preventing premature drug release. Drug release profiling (Fig. 2i) demonstrated biphasic kinetics from HCAT NPs: an initial burst phase (0–4 h) followed by sustained release. The rapid release phase likely corresponds to the surface-adsorbed HPC, while prolonged release reflects gradual nanoparticle disassembly. In contrast, free HPC showed rapid, uncontrolled release (≈80 % within 8 h). This controlled release profile of HCAT NPs mitigates off-target phototoxicity risks by extending the therapeutic window for tumor-specific accumulation while minimizing premature photosensitizer leakage.

3.3. Cascade reactions triggered by enhanced type I PDT enable self-imaging guided NO generation In vitro

3.3.1. Enhanced type I photosensitization

Leveraging its dual type I/II photodynamic properties, HPC can generate multiple ROS ($^1O_2$, H_2O_2, $\bullet O_2^-$) upon laser irradiation. Critically, we harnessed HPC's Type I photochemistry as a spatiotemporally controllable trigger to initiate cascade reactions within HCAT nanoparticles, enabling imaging-guided PDT and controlled NO release (Fig. 3a).

The distinct ROS profiles of type I ($\bullet O_2^-$) and type II ($^1O_2$) photosensitization were quantified using 1,3-diphenylisobenzofuran (DPBF) and sulfanilamide assays [25]. HCAT NPs exhibited significantly attenuated $^1O_2$ generation (Fig. 3b) but markedly enhanced $\bullet O_2^-$production (Fig. 3c) compared to free HPC, confirming preferential type I activity post-assembly. Subsequently, 1 % triton was used to destroy the nanostructure of HCAT, it can be seen that the generation capacity of $^1O_2$ was recovered after the 1 % triton was added, indicating that the self-assembly structure was the main factor that influenced the type II PDT of HCAT. Notably, although the addition of triton into HCAT solutions also induced improved $\bullet O_2^-$ production, its effect was less pronounced than that on $^1O_2$ generation. Furthermore, intact HCAT NPs also demonstrated superior $\bullet O_2^-$ production compared to HPC alone. This phenomenon may arise from multiple mechanisms:

1) Restricted oxygen diffusion within dense HCAT nanostructures limits $^1O_2$ formation (type II-dependent).
2) Enhanced non-radiative decay due to HPC's parallel stacking reduces intersystem crossing (ISC) efficiency, suppressing triplet-state formation.
3) Aggregation-promoted electron transfer *via* Cu^{2+} coordination shortens electron-transfer distances, facilitating type I reactions.

We subsequently evaluated the $\bullet O_2^-$ generation capacity of HAT, HCT, and HCA using a superoxide anion detection kit (Fig. S6). Compared with HCAT, HAT exhibited significantly reduced $\bullet O_2^-$ production, with levels comparable to HPC alone. In contrast, both Cu^{2+}-containing formulations (HCT and HCA) demonstrated markedly enhanced $O_2^-\bullet$ generation, confirming the pivotal role of Cu^{2+} in augmenting the type I photodynamic properties of HCAT NPs. Further comparative analysis revealed that HCT produced lower $\bullet O_2^-$ levels than HCAT, suggesting that L-Arg may function as a substrate to enhance the efficiency of HPC's type I photosensitizing mechanism. Meanwhile, the slightly decreased superoxide anion levels in the HCAT group compared to HCA could be attributed to TPE-4NMB's scavenging capacity for $ONOO^-$ [39], a downstream product of superoxide anion, which may facilitate partial conversion and degradation of superoxide anions.

Besides, we have employed hydroxyphenyl fluorescein (HPF) and DPBF to comparatively measure the differences in •OH (another representative ROS for Type I PDT) and $^1O_2$ generation between HAT NPs and HCAT NPs, respectively. The results demonstrated that the presence of Cu^{2+} not only significantly enhanced the $\bullet O_2^-$ production capacity of HCAT NPs but also boosted their •OH generation. In contrast, the levels of $^1O_2$ produced by the two showed little difference

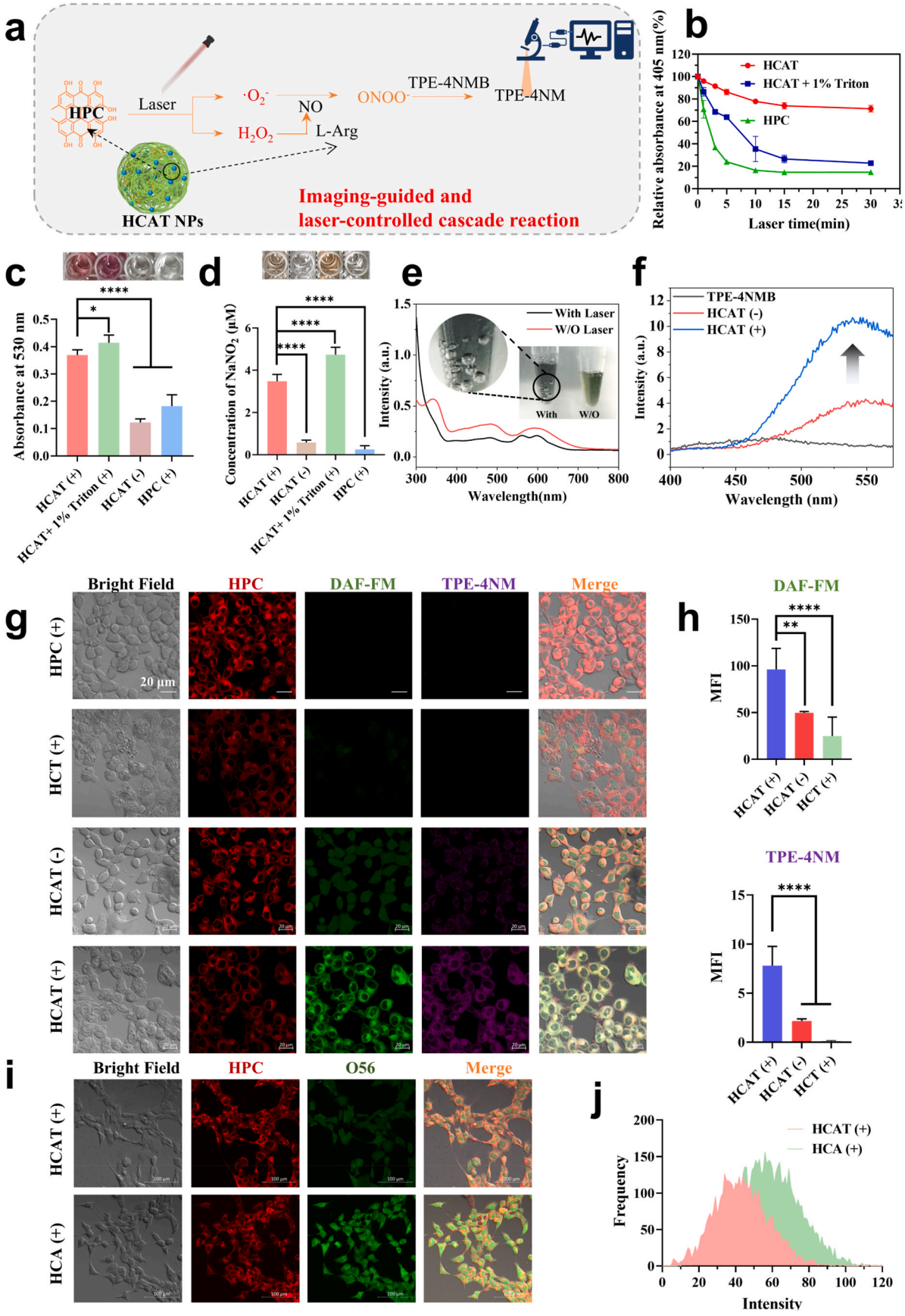

(caption on next page)

Fig. 3. Cascade reactions triggered by enhanced type I PDT enable self-imaging guided NO generation *in vitro*. a) Schematic illustration of the imaging-guide and laser-controlled cascade reaction. b) Absorbance changes of DPBF at 405 nm after being treated with HPC, HCAT, and HCAT +1 % triton (20 μg mL^{-1} as HPC) for various time periods. c) Absorbance at 530 nm of the co-incubator solution of HPC, HCAT, HCAT +1 % triton (20 μg mL^{-1} as HPC) treated with the sulfanilamide assay kit. d) The concentration of generated $NaNO_2$ after various formulations were treated with Griess reagent. e) The UV–Vis spectra and f) fluorescence spectra changes of HCAT NPs after being irradiated with a 638 nm laser (0.5 W cm^{-2}) for 10 min. g) CLSM images and h) quantification of fluorescence intensity of intracellular NO stained by DAF-FM DA (5 μ_M) after treatment with HPC, HCT, or HCAT for 4 h, 20 μg mL^{-1} as HPC. i) CLSM images and j) fluorescence intensity of intracellular $ONOO^-$ stained by BBoxiProbe@O56 (1:1000) after 4T1 cells were treated with HCA, or HCAT (20 μg mL^{-1} as HPC) for 4 h. All the statistical data are presented as mean ± SD (n = 3). Statistical significance of c), d), and h) was analyzed using one-way ANOVA. *$p < 0.05$, **$p < 0.01$, ***$p < 0.001$, ****$p < 0.0001$.

(Fig. S7). This indicates that Cu^{2+} primarily exerts a marked enhancing effect on the type I PDT activity of HCAT NPs, while having a minimal impact on their type II PDT performance.

Under alkaline conditions, Cu^+ can form a purple complex with BCA reagent, exhibiting absorbance at 562 nm, while Cu^{2+} requires reduction to Cu^+ for color development. However, laser irradiation did not significantly induce color changes in the HCAT-BCA co-incubation solution, indicating no formation of Cu^+/BCA complexes post-irradiation. This may be attributed to the significantly stronger interactions between Cu^{2+}/Cu^+ and HCAT components compared to their coordination with BCA. Even if Cu^{2+} is converted to Cu^+, it remains bound to HCAT and cannot freely coordinate with BCA, thus preventing detectable color changes. Additionally, this phenomenon indirectly indicates that Cu^{2+} is an integral part of the HCAT structure rather than being present as a free ion in the solution (Fig. S8).

Collectively, the enhanced type I characteristics of HCAT may reduce oxygen dependence during PDT, offering a strategy for hypoxia-tolerant cancer therapy and a method to augment type I activity in conventional type II PSs [14,15].

3.3.2. Laser-triggered NO generation and self-imaging

Based on the enhanced type I photosensitization of HCAT, we subsequently investigated the laser-triggered cascade catalysis of L-Arg for NO release using Griess Reagent (Fig. 3d). Results showed that HPC alone cannot produce NO, while HCAT demonstrated significant NO generation. Laser irradiation can act as an activation switch, evidenced by the gas bubble formation and UV–vis spectral changes (Fig. 3e). Notably, the NO production of HCAT and HCAT + Triton groups positively correlated to their type I photosensitization efficiency.

NO plays dual roles in regulating tumor immune escape, angiogenesis, and macrophage polarization in a dose-dependent manner [10]. Therefore, it's necessary to real-time monitor the generation of NO for precise biological modulation. As $•O_2^-$ and NO can spontaneously form $ONOO^-$, consequently, utilizing an $ONOO^-$ detection probe offers a potential strategy for the real-time monitoring of NO production by HCAT. In a previous study, we have developed TPE-4NMB, a novel probe capable of simultaneous visualization and depletion of $ONOO^-$ [31]. Here, TPE-4NMB was doped into HCAT NPs during their self-assembly process to enable real-time monitoring of NO release. As shown in Fig. 3f, upon laser irradiation, the HCAT NPs exhibited a significant increase in the fluorescence signal from the encapsulated TPE-4NMB, demonstrating its potential for visualizing NO generation.

We subsequently evaluated the cascade-driven NO production by HCAT and the detection performance of TPE-4NMB at the cellular level. Results (Fig. 3g & h) showed that laser irradiation significantly increased NO levels in the HCAT (+) group. In contrast, the HCT (+) group (lacking L-Arg) showed minimal NO production due to the disruption of the NO generation cascade, confirming L-arginine (L-Arg) as the essential component within HCAT for mediating NO production. Quantitative analysis using the commercial NO probe DAF-FM yielded results similar to those obtained from the TPE-4NMB channel within HCAT. These two detection methods exhibited a significant linear correlation (Fig. S9, $y = 0.1091x - 2.864$, $R^2 = 0.9132$), indicating HCAT's excellent self-detection capability for NO generation at the cellular level. This confirms the feasibility of using cascade-generated $ONOO^-$ to reflect NO levels in real-time in this study.

Notably, besides monitoring NO generation, the TPE-4NMB incorporated within HCAT effectively scavenged $ONOO^-$ produced during the cascade reaction (Fig. 3i & j; O56 is a commercial $ONOO^-$ probe whose fluorescence intensity positively correlates with $ONOO^-$ concentration). $ONOO^-$ is known to promote tumor metastasis by inducing endothelial cell migration, increasing vascular permeability, and facilitating the formation of immature vascular networks that provide pathways for dissemination. It also accelerates metastasis by activating MMP-mediated EMT signaling pathways [47–49]. Therefore, TPE-4NMB provides dual safeguards for enhancing the safe application of HCAT *via* visual guidance for NO release and specific scavenging of detrimental $ONOO^-$.

3.4. Cu^{2+} enhances type I photosensitization cascade-mediated NO generation through GSH depletion

Although Cu^{2+} significantly enhances the type I photosensitizing capability of HCAT at the solution level. However, tumor cells typically maintain a high redox status due to their elevated metabolic activity and adaptive responses to environmental stress and activated signaling pathways. Crucially, high intracellular glutathione (GSH) levels can buffer exogenous reactive oxygen species (ROS), protecting tumor cells from oxidative damage. Therefore, disrupting the tumor cell redox balance is essential for enhancing the efficacy of ROS-based interventions like PDT.

As illustrated in Fig. 4a, Cu^{2+} significantly diminished the absorption peak of GSH at 405 nm, indicating its potent GSH-depleting capacity. The reversible conversion between Cu^{2+} and Cu^+ enables efficient disruption of the intratumoral redox homeostasis. Under dark conditions (Fig. 4b), GSH depletion by HCAT primarily stems from Cu^{2+} activity. Although partially hindered by coordination effects and the nanoparticle physical barrier, HCAT NPs retain substantial GSH-depleting ability. Upon laser irradiation (Fig. 4c), dual depletion effects occurred from both PDT-generated ROS and Cu^{2+}. Notably, HCAT exhibits weaker GSH depletion than HCT, as some ROS participate in the NO-generating cascade. While HCA depletes GSH more effectively than HCAT, because TPE-4NMB contained in HCAT can readily scavenge the oxidizing $ONOO^-$.

Consistent with solution-level findings, cellular assays confirmed that HCAT (+) generates significantly more ROS (Fig. 4d & e) and induces stronger type I photosensitizing-mediated NO production (Fig. 4f & g) than HAT. This further demonstrates the critical role of Cu^{2+} in boosting both ROS generation and NO production by HCAT NPs.

Based on these results, we propose that Cu^{2+} enhances HCAT-mediated oxidative stress and subsequent NO generation through two primary mechanisms:

1) Enhancing Type I Photosensitization: Forming metal coordination complexes with HPC directly improves ROS generation efficiency *via* the Type I pathway.
2) Disrupting Redox Homeostasis: Depleting GSH indirectly elevates intracellular ROS levels by compromising the cellular redox balance.

Ultimately, the increased intracellular ROS levels accelerate the cascade reaction between ROS and L-Arg, effectively boosting intracellular NO production efficiency.

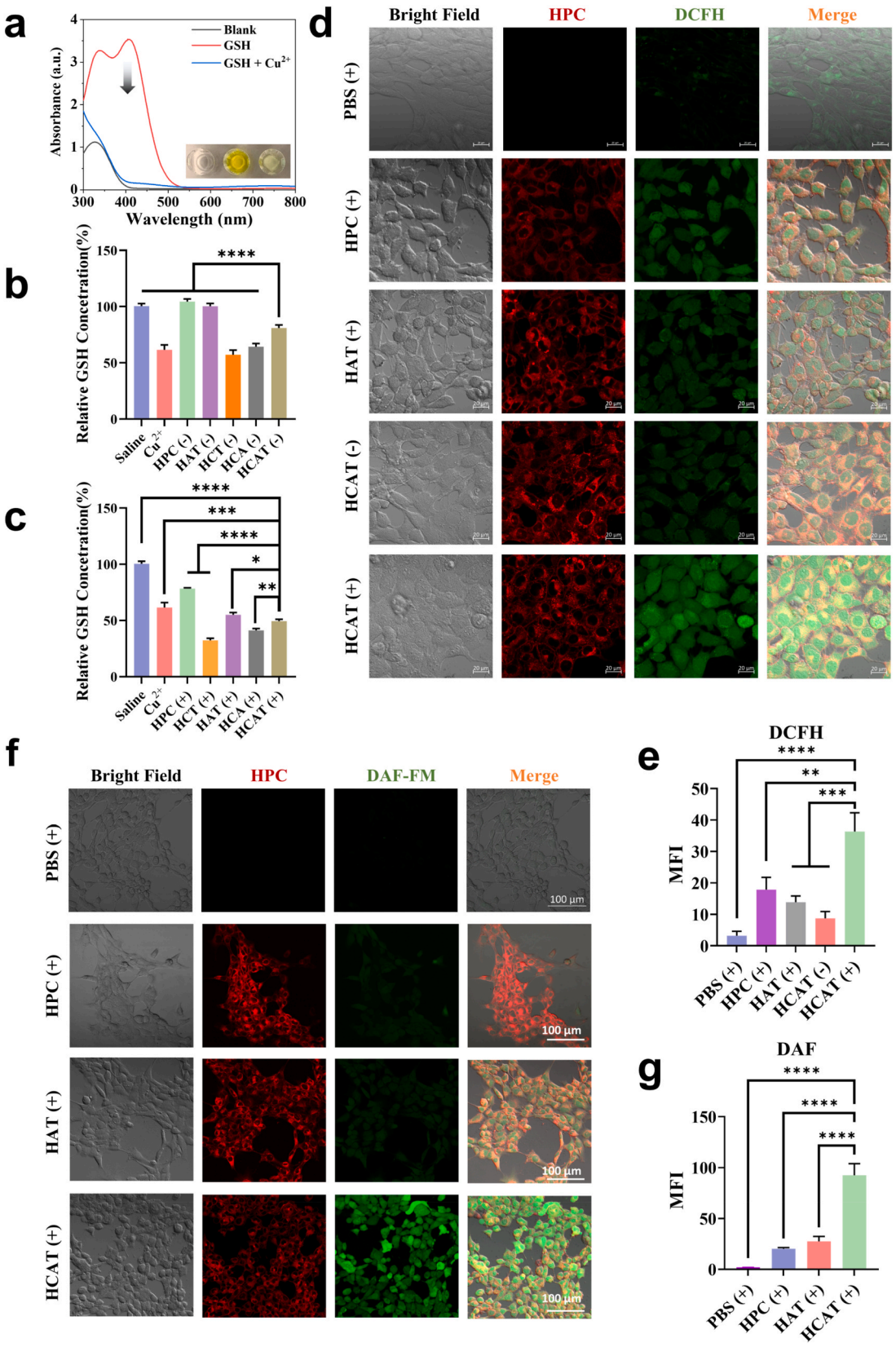

Fig. 4. Cu^{2+} enhances type I photosensitization cascade-mediated NO generation through GSH depletion. a) Images and UV–Vis spectra of residual GSH after being co-incubated with Cu^{2+}. Relative GSH concentration in the solution after reduced GSH was co-incubated with various samples b) without or c) with laser irradiation. d) Detection and e) quantification of intracellular ROS by DCFH-DA (10 μ_M) after being treated with HPC, HAT, or HCAT for 4 h, 20 μg mL^{-1} as HPC. f) CLSM images and g) quantification of fluorescence intensity of intracellular NO stained by DAF-FM DA (5 μ_M) after being treated with HPC, HAT, or HCAT for 4 h, 20 μg mL^{-1} as HPC. All the statistical data are presented as mean ± SD (n = 3). Statistical significance of b), c), f) and g) was analyzed using one-way ANOVA. *$p < 0.05$, **$p < 0.01$, ***$p < 0.001$, ****$p < 0.0001$. ns, No significant difference.

3.5. Cell uptake mechanism

4T1 cells were used to investigate the cellular uptake behavior of HCAT NPs. As shown in Fig. S10a and S10b, HCAT NPs predominantly localized to mitochondria post-internalization, contrasting with free HPC accumulation in lysosomes. Given mitochondria's critical role as energy-producing organelles, HCAT activation within this compartment may inflict irreversible damage on tumor energy metabolism. Subsequent mechanistic investigations focused on elucidating the uptake pathways (Fig. S10c). Incubation at low temperatures (4 °C) markedly altered the intracellular distribution of HCAT, resulting in the retention of particles on the cell membrane surface, thereby indicating that the internalization of HCAT is an energy-dependent process. Pharmacological inhibition using chlorpromazine, which impedes clathrin-coated pit formation, significantly diminished intracellular HCAT levels, whereas methyl-β-cyclodextrin, an inhibitor of caveolin-dependent endocytosis, exhibited minimal effect [17]. These findings imply that clathrin-mediated endocytosis constitutes the primary mechanism for the uptake of HCAT nanoparticles.

3.6. Enhanced PDT efficacy via type I photosensitization

MTT assays and live/dead cell staining were utilized to assess the cytotoxicity of HCAT. As illustrated in Fig. 5a, HCAT achieved a significantly lower IC_{50} (0.28 μg mL^{-1}) compared to HPC (1.77 μg mL^{-1}), which can be attributed to the synergistic effect of the cascade reaction, while individual components Cu^{2+}, L-Arg, or TPE-4NMB alone exhibited minimal cytotoxicity to 4T1 cells within the 0–10 μg mL^{-1} range (Fig. S11) [39]. Meanwhile, the cytotoxicity of HCAT displayed significant laser-dependent characteristics, suggesting a strong correlation with HPC-mediated photosensitization (Fig. S12). Notably, PDT efficacy of HPC and HAT showed pronounced oxygen dependence, while cytotoxicity of HCT, HCA, and HCAT exhibited reduced oxygen sensitivity (Fig. 5b and c). This distinction confirms that HPC/HCA-mediated cytotoxicity primarily originates from Type II photosensitization, whereas HCAT/HCT/HCA-induced cytotoxicity predominantly derives from Type I mechanisms. These findings highlight HCAT's therapeutic potential for targeting deep-seated hypoxic tumors located away from vascular networks.

The live/dead assay was further conducted to confirm the type I PDT effect of HCAT in killing 4T1 cells. As shown in Fig. 5d, the PDT effect of HPC and HAT was significantly affected by oxygen concentration. Under hypoxia, their cytotoxicity to 4T1 cells was obviously weakened, and only sporadic cell death occurred. However, the cytotoxicity of HCA, HCAT and HCAT was less affected by oxygen concentration, and more than half of cells were still apoptotic under hypoxia. It was proven that Cu^{2+}-enhanced Type I photosensitization enables effective tumor cell elimination in hypoxic microenvironments, particularly advantageous for targeting deep-seated or poorly vascularized tumors.

3.7. In vitro penetration of NO-driven nanomotor in cellular models

Inadequate therapeutic accumulation in deep-seated tumor regions constitutes a critical efficacy barrier, exacerbated by hypoxia-enhanced invasiveness and interstitial hypertension impeding drug delivery. Nanomotors, which convert environmental energy into mechanical motion, represent a promising strategy to overcome interstitial pressure and enhance penetration [20,22]. Recent studies demonstrate their

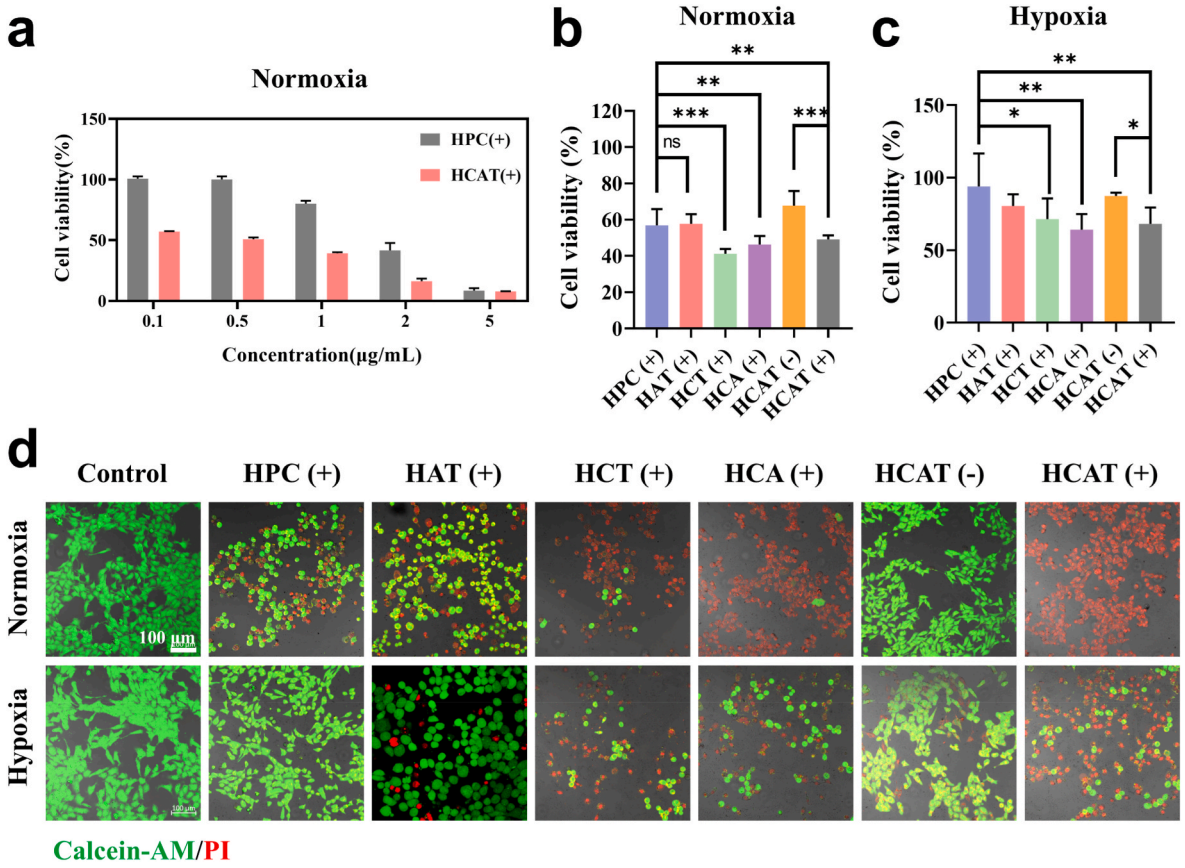

Fig. 5. Enhanced PDT efficacy *via* type I photosensitization. a) The cytotoxicity of HPC and HCAT against 4T1 cells with various concentrations. Cytotoxicity of different formations against 4T1 cells under b) normoxia or c) hypoxia conditions, 1 μg mL^{-1} as HPC. d) CLSM images of Calcein-AM and propidium iodide stained 4T1 cells with different treatments (20 μg mL^{-1} as HPC). Scale bars = 100 μm. All the statistical data are presented as mean ± SD (n = 3). Statistical significance of b), and c) was analyzed using one-way ANOVA. *$p < 0.05$, **$p < 0.01$, ***$p < 0.001$. ns, No significant difference.

capacity to facilitate micron-scale T-cell infiltration, suggesting potential for amplifying PDT-mediated immunotherapy [17].

Herein, laser-triggered NO generation by HCAT was revealed to significantly enhance the motility of nanomotor. Under dark conditions, HCAT exhibited random Brownian motion (Fig. 6a & Movie S1) with a displacement velocity of 28.3 pixel s^{-1}, while laser irradiation induced rapid directional chemotaxis (Fig. 6a & Movie S2), increasing velocity by ~21-fold–594.6 pixel s^{-1}. This directional propulsion correlated with localized ROS accumulation from type I photosensitization at the irradiation site.

Although laser guidance partially directed nanomotor motion, penetration efficacy within 3D tumor structures remained limited. Necrotic regions located in deep tumor tissues due to nutrient deprivation were confirmed *via* 3D spheroid live/dead staining (Fig. 6b). HPC's inherent necrotic tissue affinity provided a targeting mechanism to augment nanomotor distribution [44,50]. As shown in Fig. 6b, the HPC-stained regions in 3D tumor spheroids demonstrate significant spatial overlap with PI-stained areas (apoptotic and necrotic cell marker), further confirming the feasibility of using HPC to target deeply located necrotic cells.

Penetration depth assessment in multicellular tumor spheroid (MTSs) demonstrated superior performance of laser-activated HCAT (+)

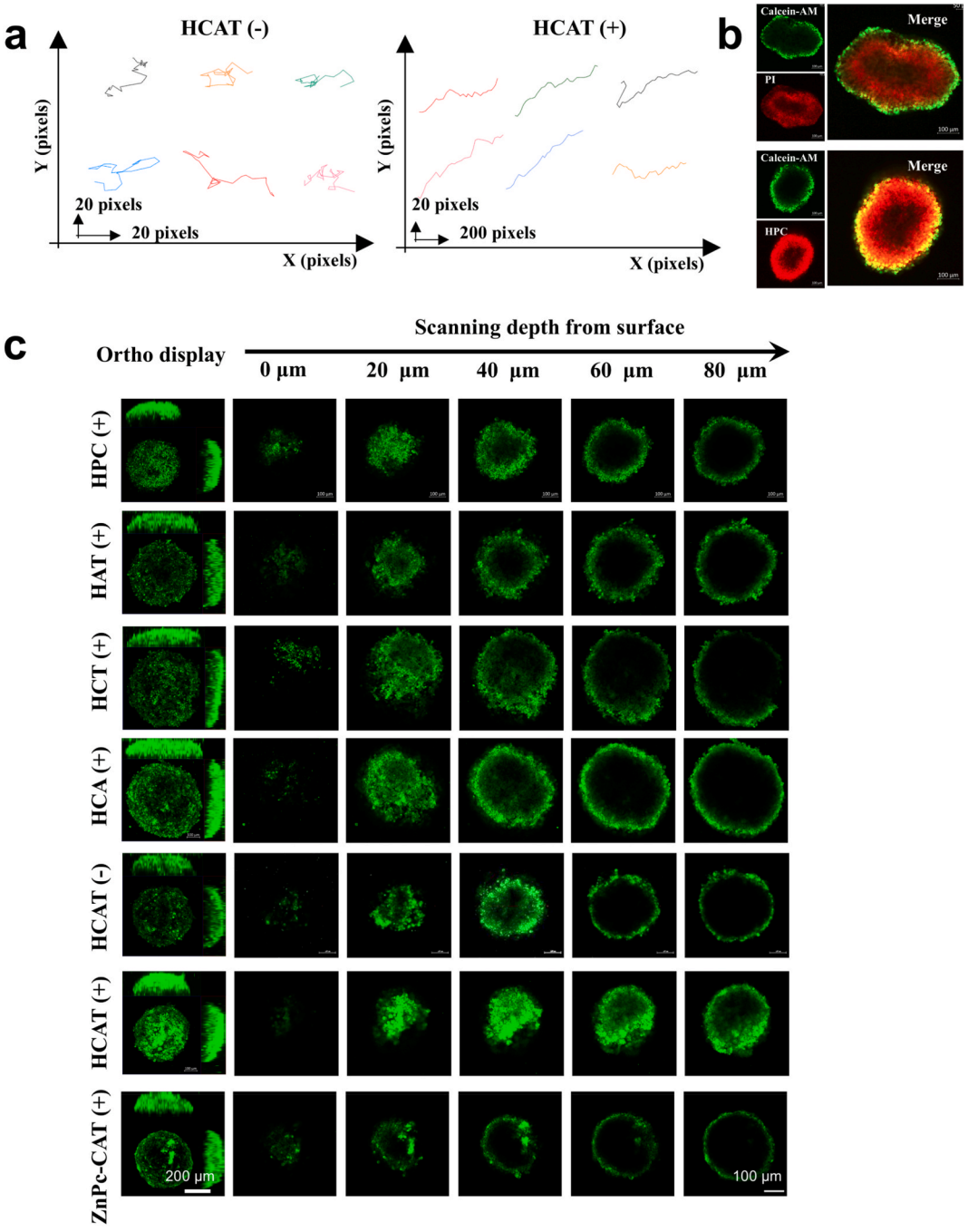

Fig. 6. *In vitro* penetration of NO-driven nanomotor in cellular models. a) Representative motion trajectories of HCAT NPs in the dark or upon laser irradiation (638 nm, 0.5 W cm^{-2}, 1 min). b) Fluorescence images of MTSs stained by Calcein-AM (2 μ_M)/PI (8 μ_M) or Calcein-AM (2 μ_M)/HPC (20 μg mL^{-1}). c) CLSM z-scanning images of 4T1 MTSs after different treatments for 4 h (+) and (−) indicate whether the group was exposed to laser irradiation (638 nm, 0.5 W^{-2}, 1 min) or not, respectively.

(Fig. 6c), exhibiting significantly higher fluorescence intensity at 60 μm depth *versus* other groups. Non-irradiated HCAT (−) and laser-irradiated HCT (+) showed reduced penetration, confirming the critical role of NO in propulsion. HCA NPs showed diminished penetration due to structural instability (Fig. S2). HAT (minimal NO generation) relied solely on HPC's necrosis targeting, exhibiting penetration comparable to free HPC. As a typical type II photosensitizer, ZnPc cannot activate the cascade reaction to generate NO upon laser irradiation, nor does it possess the ability to target necrotic cells [44]. Therefore, the ZnPc-CAT group can be used as a control to help us to further illustrate the importance of both necrotic cells targeting and NO gas propulsion for achieving deep drug penetration. As anticipated, ZnPc-CAT (+) demonstrated the shallowest penetration (Fig. 6c).

Collectively, these findings demonstrate that laser-induced NO generation effectively propels HCAT NPs into deep tumor regions. Meanwhile, necrotic cells in hypoxic zones provide an intrinsic guidance mechanism, enabling necrosis-targeting chemotaxis for directional tumor penetration. This establishes a positive feedback loop between targeting necrotic tissues to enhance its penetration into deep tumor regions and inducing necrosis within these deep-seated tumor areas, offering a novel strategy for eliminating deep-seated refractory tumors.

3.8. Immunogenic cell death and dendritic cell activation mediated by HCAT nanomotors in vitro

The exposure of calreticulin (CRT) and the extracellular release of high mobility group box 1 (HMGB1) were observed using CLSM. As is depicted in Fig. 7a & c, 4T1 cells in the control group (Ctrl) exhibited minimal membrane CRT expression, while all drug-treated groups showed increased CRT fluorescence intensity. Notably, the HCAT (+) and HCA (+) groups demonstrated comparable CRT levels, with increases of 7.14-fold and 7.29-fold over the control group, respectively. The HCT group showed moderate CRT expression, followed by the HPC, HCA, and HCAT groups. Importantly, the HCT (+) group exhibited lower fluorescence intensity compared to the HCAT and HCA groups, suggesting that NO, in addition to ROS derived from type I PDT, plays a role in CRT translocation. The HAT (+) group, which relies on HPC-mediated Type II photosensitization post-disassembly, showed CRT levels similar to those of the HPC (+) group.

HMGB1, a nuclear protein, is released into the extracellular space during ICD. As illustrated in Fig. 7b & d, the HCAT (+) and HCA (+) groups exhibited significantly reduced nuclear HMGB1 fluorescence compared to other groups. The HCT group maintained higher nuclear HMGB1 levels due to the absence of NO-mediated synergistic effects, while the HAT and HPC groups displayed similar profiles.

ATP secretion, assessed using an ATP assay kit (Fig. 7e), indicated that all nanoparticle groups facilitated ATP release from 4T1 cells. Consistent with the findings on CRT and HMGB1, the HCAT (+) and HCA (+) groups demonstrated 12-fold and 10-fold higher ATP levels than the HPC (+) group, respectively. The HCT (+) group exhibited significantly lower ATP concentrations than the HCAT (+) and HCA (+) groups, suggesting that NO has a greater influence on ATP release compared to ROS. These results all confirmed that HCAT (+) potently induces ICD *via* Cu^{2+}-enhanced Type I photosensitization and NO generation.

To further validate HCAT-induced ICD in promoting DCs maturation, 4T1 tumor cells were co-incubated with various treatment formulations prior to co-culture with immature DCs. Flow cytometry analysis of $CD11c^{+}IA\text{-}IE^{+}$ costimulatory molecule expression revealed DCs maturation profiles consistent with immunofluorescence findings (Fig. 7f and g). While HPC (+), HAT (+), and HCT (+) treatments induced moderate DCs maturation capacity, HCAT (+) and HCA (+) demonstrated significantly enhanced efficacy, elevating mature DCs proportions from 22.9 % (control) to 37.1 % and 39.0 %, respectively. Critically, laser irradiation was essential for HCAT-mediated DCs maturation.

Collectively, these results establish that HCAT (+) exhibits significant *in vitro* antitumor immunotherapeutic potential, wherein laser-activated photodynamic effects initiate adaptive immune responses through DCs' maturation.

3.9. Self-reporting the drug distribution and NO release In Vivo

To validate HCAT's *in vivo* self-reporting capabilities, near-infrared (NIR) fluorescence of HPC was leveraged to monitor drug biodistribution in 4T1 tumor-bearing mice. The *in vivo* and *ex vivo* imaging revealed similar overall biodistribution and metabolic profiles between HCAT NPs and free HPC, while HCAT demonstrated 1.5-fold higher tumoral fluorescence intensity at 6 h post-administration, indicating HCAT NPs possess more superior tumor-targeting efficiency than free HPC (Fig. 8a-e). Progressive tumor accumulation occurred within 0–6 h, followed by gradual clearance and stabilization at 24 h—establishing 6 h as the optimal PDT irradiation timepoint. Metabolic analysis revealed that the liver and kidneys serve as the primary clearance organs for HCAT (Fig. 8b), with peak hepatic/renal fluorescence at 6 h and signal elimination by 48 h, indicating minimal accumulative toxicity risk. This tumor-selective accumulation coupled with efficient clearance positions HCAT as a spatiotemporally controllable therapeutic platform.

Based on the *in vitro* validation of TPE-4NMB-mediated NO detection, we assessed the *in vivo* NO self-monitoring capabilities of HCAT using 4T1 breast cancer-bearing BALB/c mice, and employing the commercial DAF-FM DA probe as a reference standard. As illustrated in Fig. 8f-j, significantly enhanced TPE-4NMB fluorescence was observed in laser-irradiated tumors *versus* non-irradiated controls, with signal intensity progressively increasing over 24 h post-irradiation. Linear regression analysis revealed a strong correlation between the signals of TPE-4NM and DAF-FM (Fig. 8k, $R^2 = 0.9035$), thereby confirming the high accuracy of HCAT for real-time *in vivo* NO tracking.

3.10. Self-amplified necrotic targeting and deep tumor penetration In Vivo

Encouraged by the high affinity of HPC to necrotic cells and its ability in inducing cell apoptosis, the concept of "necrosis-targeting to necrosis-inducing" self-amplifying cycle was proposed [44,50].

Firstly, as depicted in Fig. S13, the necrotic organization of the tumor was mainly located in the center, while the fluorescence of HPC was concentrated in the same spatial position, indicating that HPC still retains excellent deep necrotic tissue affinity *in vivo*, and its spatial distribution provides an avenue for facilitating the nano-drugs to deep tumor penetration. Subsequently, to validate targeting efficacy, paclitaxel-induced pre-necrotic tumors were established. HCAT exhibited 1.6-fold higher accumulation in pre-necrotic *versus* non-necrotic tumors, while ZnPc-CAT accumulation decreased to 0.89-fold (Fig. 9a-c). The phenomenon can be attributed to the discrepancy: 1) HPC-mediated necrotic targeting enhancing HCAT delivery to necrotic regions; 2) Reduced cellular viability impairing the cell uptake of ZnPc-CAT; 3) Elevated interstitial pressure post-paclitaxel treatment impaired the transport of ZnPc-CAT.

Deep tumor regions, characterized by hypoxia and nutrient deprivation, exhibit higher necrosis rates and increased aggressiveness of residual tumor cells. HCAT's Type I photosensitization minimizes oxygen dependency, enabling effective PDT even in hypoxic microenvironments. This property, combined with necrosis targeting, creates a synergistic "necrosis-induction" to "enhanced targeting" cycle.

Histological analysis (Fig. 9d) demonstrated pan-tumoral HPC distribution in HCAT (+)-treated tumors *versus* peripheral ZnPc-CAT localization. Superior penetration depth also occurred relative to HCA/HAT/HCT groups, which can be attributed to the dual mechanisms: 1) HPC's necrosis affinity directing nanomotor distribution; 2) NO-driven propulsion overcoming interstitial barriers.

In summary, HCAT integrates necrotic targeting with NO-driven propulsion for deep-seated tumor eradication, establishing a translatable paradigm for refractory solid tumors.

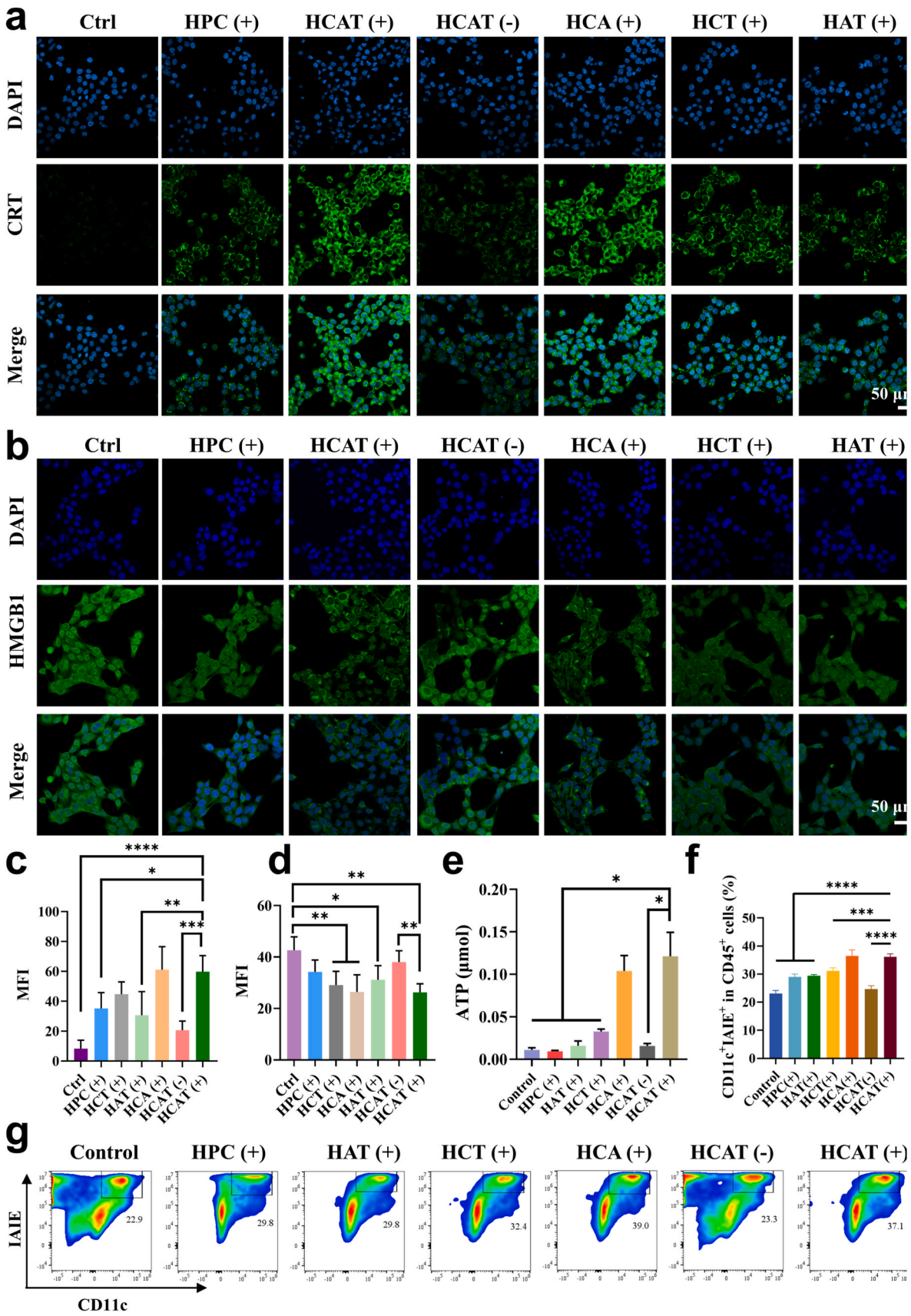

Fig. 7. Immunogenic cell death and antigen presentation *in vitro*. Immunofluorescence analysis of a) CRT and b) HMGB1 exposure in 4T1 cells after different treatment. Quantitative analysis of c) CRT, d) HMGB1 and e) ATP release patterns of 4T1 cells exposed to various formulations. f) The maturation DCs rate of BMDCs co-cultured with 4T1 cells under various treatments. g) *In vitro* flow cytometry analysis of matured BMDCs. All the statistical data are presented as mean ± SD (n = 3). Statistical significance of d), e), f) and g) were analyzed using one-way ANOVA. *$p < 0.05$, **$p < 0.01$, ***$p < 0.001$, ****$p < 0.0001$.

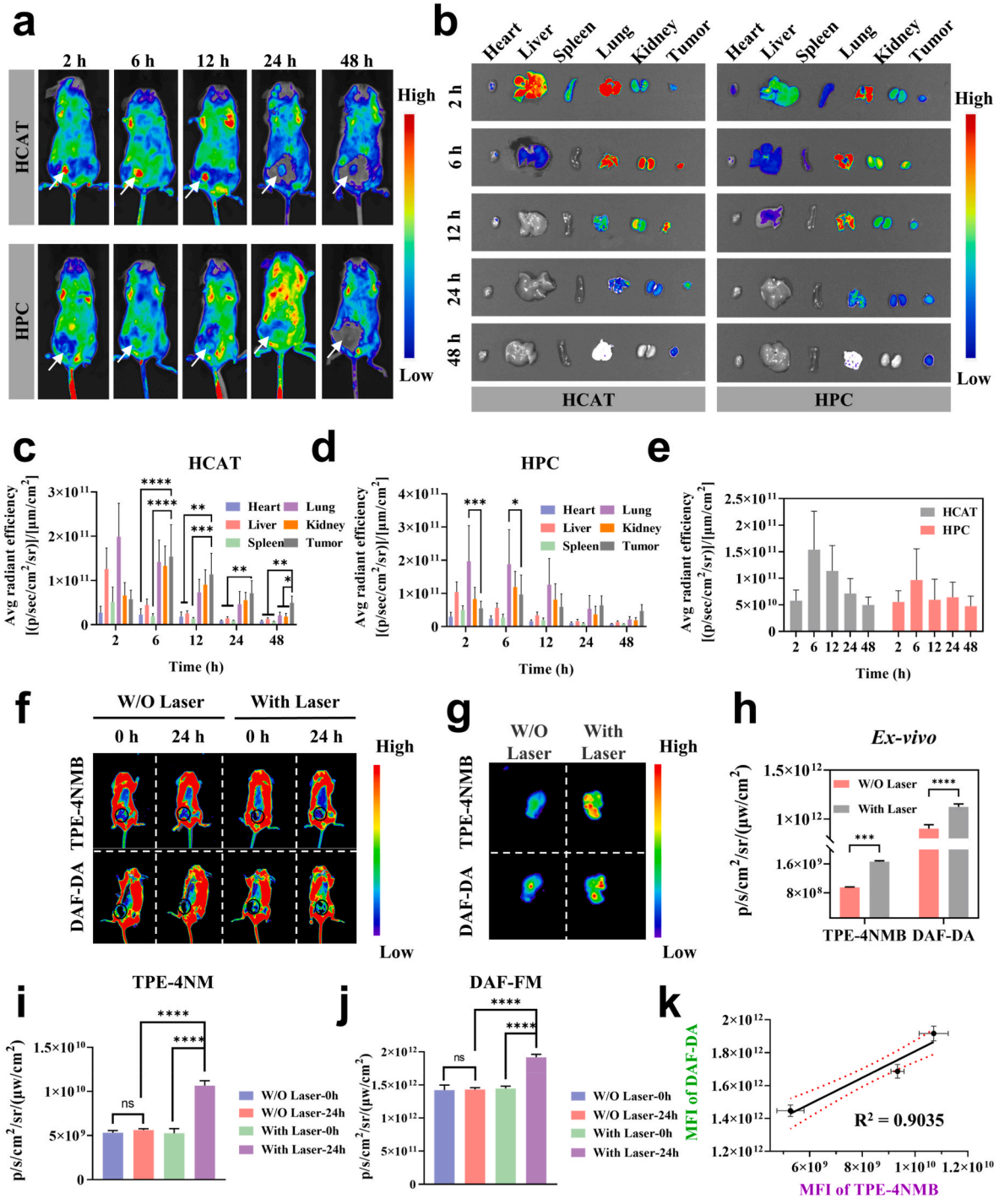

Fig. 8. Self-reporting the drug distribution and NO release *in vivo*. a) Time-dependent fluorescence imaging of 4T1-bearing mice that were intravenously administered with free HPC or HCAT NPs (20 μg mL^{-1} as HPC). b) *Ex vivo* fluorescence imaging and c, d, e) quantification of the major organs and tumors after intravenous injection at various times. f) *In vivo* fluorescence imaging of the living 4T1 tumor-bearing mice after being irradiated with a 638 nm laser for 10 min and then imaged at 24 h. g) *Ex vivo* fluorescence imaging and h) quantification of the tumors after intravenous injection with 24 h. Quantifications of the tumors' fluorescence *via* the i) TPE-4NM channel or j) DAF-FM channel *in vivo*. k) Correlation analysis between the mean fluorescence intensity (MFI) of TPE-4NM and MFI of DAF-FM at various times *in vivo*. All the statistical data are presented as mean ± SD (n = 3). Statistical significance of h) was analyzed using two-tailed Student's t-test; Statistical significance of i), j) was analyzed using one-way ANOVA. ***$p < 0.001$, ****$p < 0.0001$.

3.11. *In Vivo PDT efficacy of HCAT*

To evaluate the *in vivo* PDT efficiency of HCAT, xenografted 4T1 tumor-bearing mice were randomly divided into seven groups for treatments (Saline, HPC (+), HCAT (+), HCT (+), HCA (+), HCAT (+)). All the mice were treated according to the timeline shown in Fig. 10a. As shown in Fig. 10b, the treatment of HPC alone could not efficiently inhibit tumor growth, while HCT, HAT, HCA showed moderate efficacy, and HCAT exhibited the most potent tumor suppression at the study endpoint. Notably, no significant body weight loss was observed in HCAT-treated mice throughout the treatment period (Fig. 10c), indicating favorable biosafety.

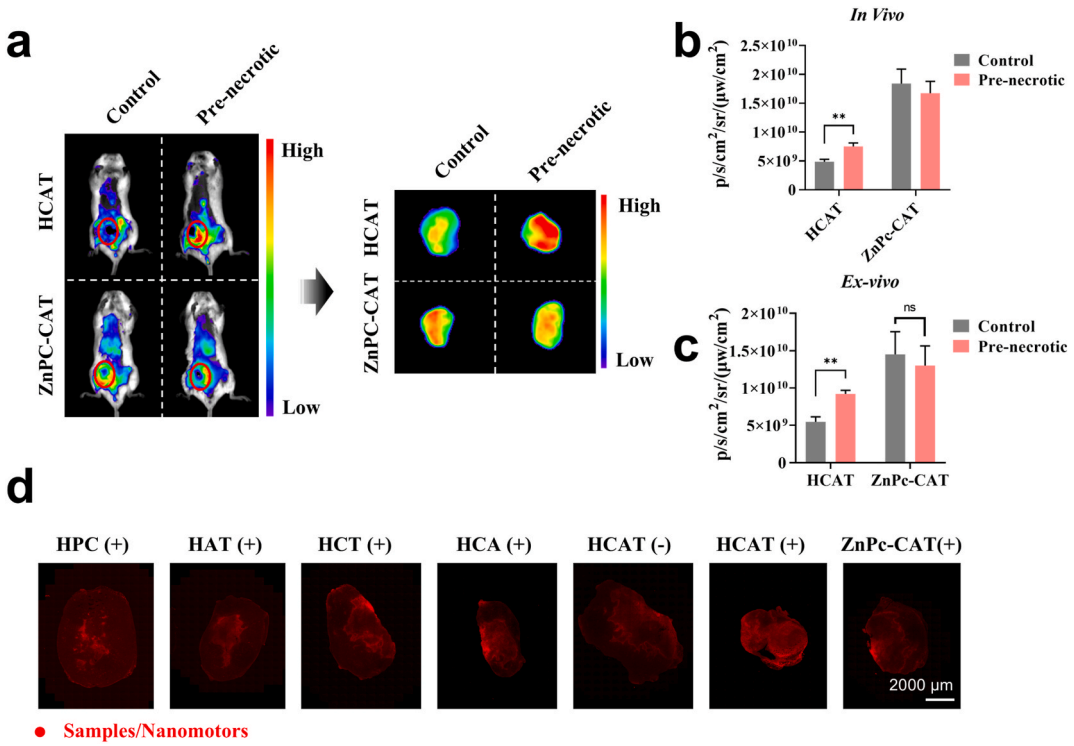

Fig. 9. Self-amplified necrotic targeting and deep tumor penetration *in vivo*. *In vivo* and *ex-vivo* a) fluorescence imaging and (b, c) quantification of the tumors after intravenous injection with HCAT or ZnPc-CAT (2 mg kg^{-1} as HPC, 100 μL) for 6 h, and with a 24 h pretreatment of PTX (2 mg kg^{-1}, 60 μL) to elevate tumor necrosis. d) The fluorescence distribution of various formations in the tumor slices at the maximum tumor diameter. All the statistical data are presented as mean ± SD (n = 3). Statistical significance of b), and c) was analyzed using two-tailed Student's t-test. $^{**}p < 0.01$. ns, No significant difference.

Immunohistochemical and immunofluorescence analyses were employed to investigate the antitumor mechanisms (Fig. 10d). H&E staining revealed that the HCAT (+) group exhibited the most extensive tumor necrosis, characterized by nuclear pyknosis, predominant hyperchromatic cytoplasm, and vacuolar degeneration. TUNEL assay results demonstrated the highest apoptotic induction in this group, with intertumoral fluorescence intensity 1.6-fold higher than the HPC group, confirming the superior antitumor efficacy of HCAT (+) (Fig. S14a). Ki67 staining indicated that the photosensitizer HPC group significantly reduced cellular proliferative activity compared to the control group, showing photodynamic necrosis capacity (Fig. S14b). However, limited TUNEL-positive apoptotic cells suggested suboptimal PDT efficacy of free HPC, potentially due to the type II PDT impairment under hypoxic tumor microenvironments. HAT (+) and HCT (+) groups showed enhanced proliferation inhibition and apoptosis induction compared to free HPC, indicating beneficial effects of Cu^{2+} and L-Arg supplementation. Nevertheless, their antitumor efficacy remained inferior to HCAT (+), likely due to the absence of synergistic Cu^{2+}-NO interactions. The HCA group, despite containing Cu^{2+} and L-Arg, exhibited compromised tumor targeting and reduced *in vivo* efficacy, attributable to structural instability from deficient TPE-4NMB-mediated hydrophobic interactions.

3.12. Antitumor mechanism analysis of HCAT

RNA-sequencing analysis further elucidated the anti-tumor mechanism of HCAT *in vivo*. As illustrated in Fig. S15a, Volcano plot analysis revealed significant alterations in gene expression profiles between the saline and HCAT (+) treated murine tumor tissues, with 468 upregulated genes (red dots) and 632 downregulated genes (blue dots). Fig. S15b showed the overall differentially expressed genes (DEGs) in each group, revealing substantial disparities in mRNA regulation between the HCAT group and saline group. Subsequently, to investigate the effect of HCAT treatment on cellular signaling mechanisms, we performed Gene Ontology (GO) enrichment analysis on differentially expressed genes (Fig. S15c and S15d). The genes associated with positive regulation of immune system process and positive regulation of leukocyte activation were up-regulated in the HCAT group, while the terms related to regulation of cellular metabolic process, cellular response to hypoxia and regulation of cell migration were down-regulated. Furthermore, Kyoto Encyclopedia of Genes and Genomes (KEGG) pathway analysis identified significant enrichment in PI3K-AKT, JAK-STAT, TNF, p53, HIF-1α, MAPK, and antigen processing and presentation signaling pathways were enriched, which were related to tumor microenvironment, tumor immunoregulation, tumor cell proliferation and apoptosis (Fig. S15e). Usually, Cytokine-cytokine receptor interaction illustrates the successful activation of innate immune response, indicating that PDT induces robust ICD. PI3K-Akt signaling pathway is related to the inhibition of mTOR pathway, which confirms that HCAT NPs down-regulated proteins related to the reduced level of GSH [51]. Collectively, transcriptomic profiling reveals that HCAT efficiently activates the ICD of tumor cells, remodels the tumor immune microenvironment and enhances cytotoxicity through coordinated modulation of immunostimulatory, metabolic, and apoptotic signaling networks.

3.13. Immune response In Vivo

Encouraged by the *in vitro* results and the RNA-sequencing analysis, we comprehensively evaluated the immune-modulatory function of HCAT *in vivo*. Immunofluorescence analysis of tumor tissues revealed significant upregulation of ICD-related markers in the HCAT (+) group. As shown in Fig. 11a & c, CRT (red fluorescence) exposure increased nearly 20-fold compared to the control group and 10-fold relative to the HPC group. Conversely, HMGB1 expression decreased markedly in HCAT (+) tumors (Fig. 11a and d), confirming robust ICD induction *in*

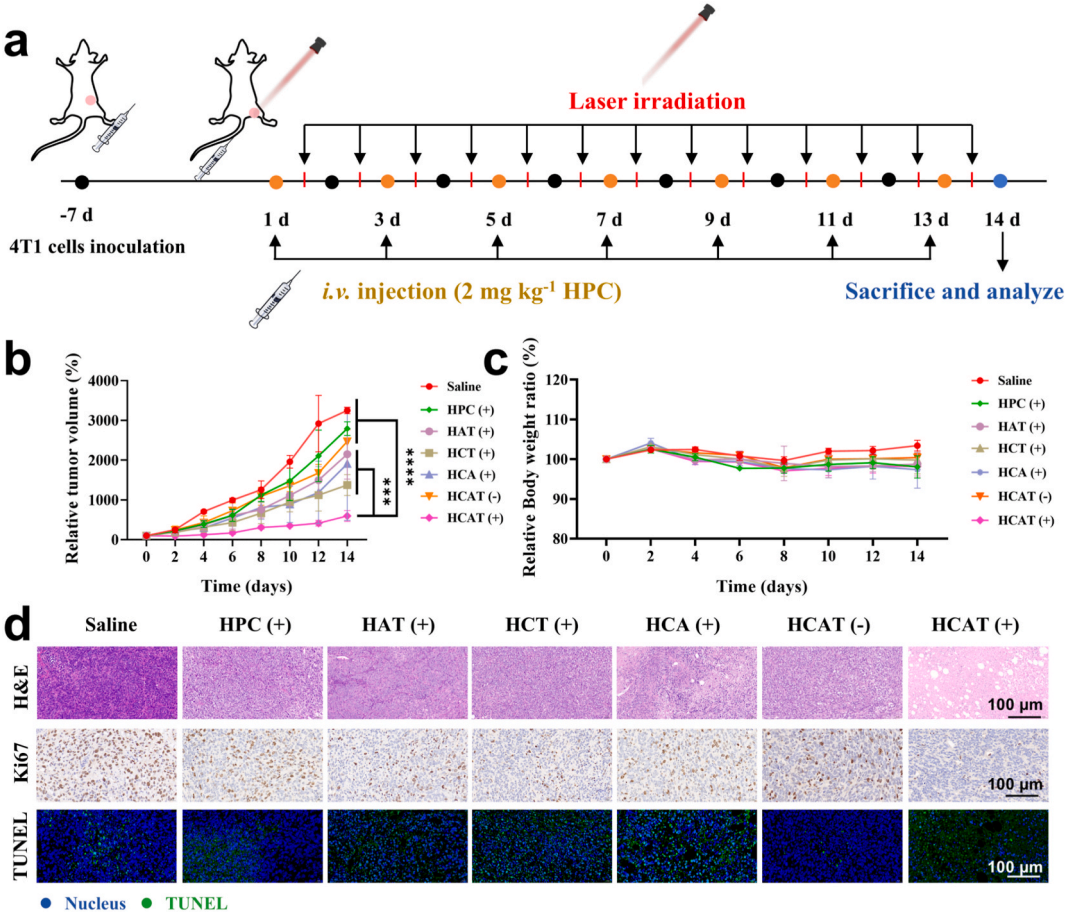

Fig. 10. *In Vivo* PDT Efficacy of various formations. a) Schematic illustration showing the timeline of the efficacy study. b) Relative tumor volume and c) relative body changes of 4T1 bearing mice during the treatment (2 mg kg^{-1} as HPC, 100 μL), (n = 10). d) H&E, Ki67, and TUNEL assay after different treatments (n = 3). Data are presented as mean ± SD. Statistical significance of b) was analyzed using two-way ANOVA. ***$p < 0.001$, ****$p < 0.0001$.

vivo. Notably, HAT/HCA/HCT groups showed attenuated ICD marker expression *in vivo* compared to *in vitro* results, maybe due to the complexity of *in vivo* ICD processes involving drug delivery efficiency, intertumoral penetration, and cytotoxicity—factors absent in 2D cell models. Mechanistically, HCAT NPs leveraged the EPR effect for passive tumor accumulation (*vs.* HPC/HCA), followed by HPC-guided necrosis targeting and Cu^{2+}-enhanced NO generation for deep intratumorally penetration (*vs.* HCT). Combined with Cu^{2+}-potentiated type I photodynamic effects and HPC-mediated type II PDT (*vs.* HAT), this synergistic design achieved superior cytotoxicity and ICD induction, correlating with significantly elevated intertumoral $CD8^+$ T cell infiltration in HCAT (+) tumors (Fig. 11a & e).

ICD-released antigens stimulate the maturation of DCs in lymph nodes, initiating adaptive antitumor immunity. Flow cytometry analysis confirmed HCAT (+) induced the most robust DCs maturation—achieving 27.5 % mature DCs—representing a 3.58–4.54-fold enhancement over comparator groups (Fig. 11b and f). Mature DCs subsequently primed $CD8^+$ T cells, driving profound intratumoral infiltration (20.2 % in HCAT (+) tumors; 10-fold *vs.* controls; 4-fold *vs.* HPC (+); Fig. S16a and S16b). This $CD8^+$ T-cell dominance underscores its pivotal role in HCAT's efficacy. Critically, HCAT exceeded HCT (+) in T-cell accumulation (20.2 % *vs.* 8.3 %), demonstrating NO's dual function in enhancing tumor penetration and reversing immunosuppression.

Beyond $CD8^+$ T cells, HCAT (+) also significantly increased natural killer (NK) cell infiltration compared to other groups (Fig. S16a and S16c), while the structural instability of HCA compromised its NK-stimulatory capacity. Simultaneously, HCAT (+) profoundly reduced immunosuppressive cell populations. Regulatory T cells (Tregs) infiltration decreased to 7.24-fold and 4.10-fold of control and HPC, respectively (Fig. S16a and S16d). While myeloid-derived suppressor cells (MDSC) proportions exhibited a sharp reduction (Fig. S16e). These coordinated changes—enhanced cytotoxic lymphocytes with diminished immunosuppressive cells—confirm HCAT's capacity to remodel the tumor immune microenvironment.

Collectively, HCAT NPs integrate photodynamic therapy, NO gas therapy, and necrosis-targeting to induce potent ICD, activate DC-mediated adaptive immunity, and reprogram the tumor immune microenvironment, offering a multimodal strategy for enhanced antitumor immunity.

3.14. *Eradicating metastatic seeds via $ONOO^-$ scavenging and vascular normalization*

Pulmonary metastasis remains a primary cause of breast cancer mortality. To evaluate the antimetastatic efficacy of nanotherapeutics, lung tissues were histopathologically examined *via* H&E staining post-treatment. While all nano-formulations demonstrated anti-metastatic activity, HCAT (+) treatment showed the most potent efficacy, with sparsely distributed metastatic foci (Fig. S17a and S17b). Moderate suppression was observed in HCT (+) and HAT (+) groups; whereas HCA (+) displayed substantially more nodules than HCAT (+) ($p < 0.01$), validating that structural stability and $ONOO^-$ depletion is critical for effective metastasis prevention.

Immunohistochemical analysis was used to elucidate the underlying mechanisms (Fig. S17c). CD31 staining indicated substantial vascular disruption in HPC and HCT groups, with significantly reduced CD31

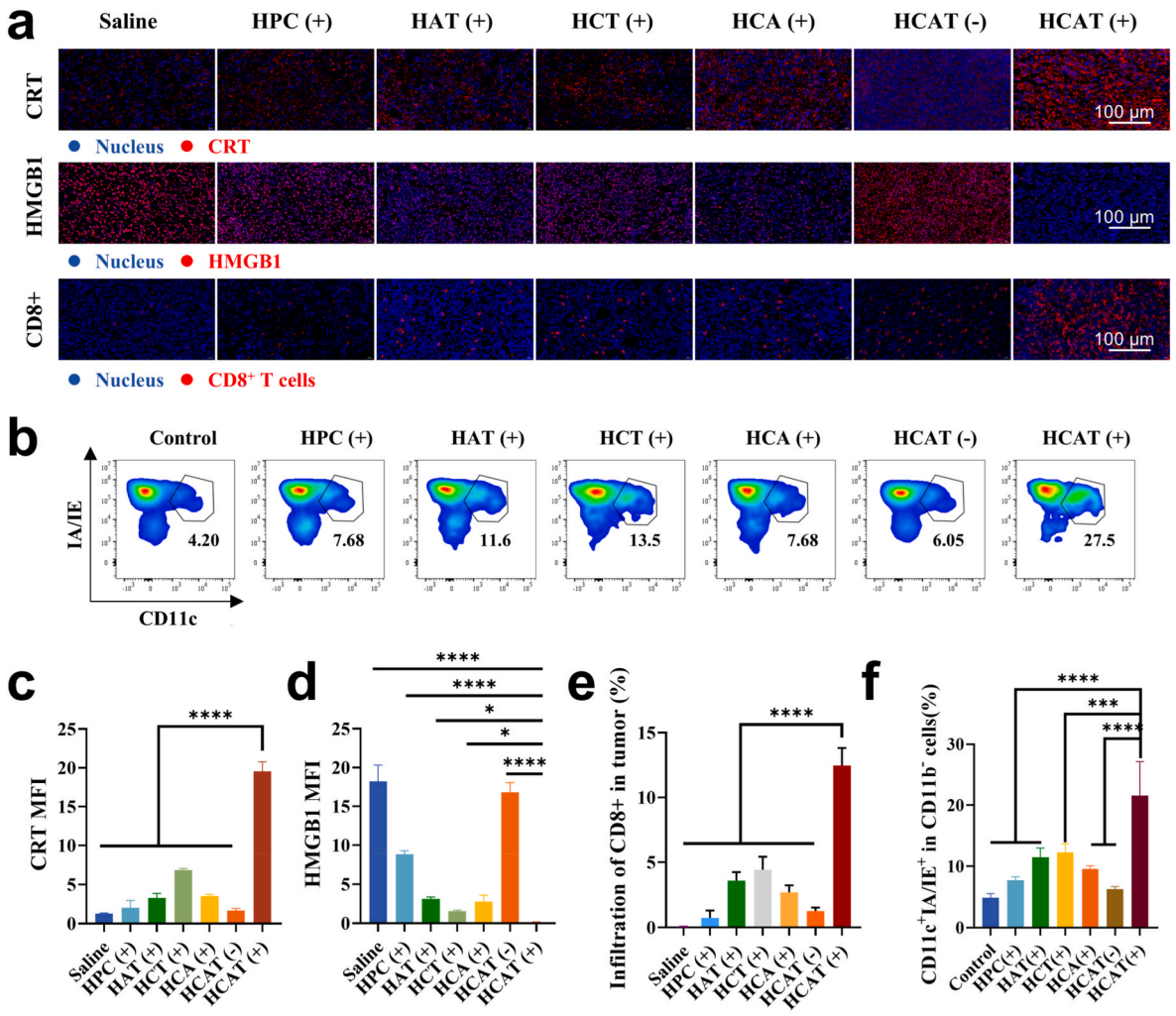

Fig. 11. ICD effect *in vivo*. a) CRT expression, HMGB1 release profiles and infiltrating of $CD8^+$ T cells in the tumors after being treated with different formulations on day 14. b) The flow cytometric analysis of DCs' antigen presentation ability in lymph nodes with various treatments. The quantitative data of c) CRT, d) HMGB1, e) maturation DCs (CD11c + IA/IE+), and f) infiltration of $CD8^+$ T cells. All the statistical data are presented as mean ± SD (n = 3). Statistical significance of c), d), e), and f) was analyzed using one-way ANOVA. $^*p < 0.05$, $^{***}p < 0.001$, $^{****}p < 0.0001$.

immunoreactivity concomitant with elevated HIF-1α expression *versus* controls. Paradoxically, HCAT reduced CD31 expression while simultaneously decreasing HIF-1α levels, indicating vascular normalization through improved mural cell coverage caused by NO [52]. $ONOO^-$ can activate pro-matrix metalloproteinases (pro-MMPs), converting latent TGF-β complexes into immunosuppressive isoforms that promote EMT and tumor immune evasion. It can be seen that groups containing the $ONOO^-$ scavenger TPE-4NMB (HAT/HCT/HCAT) showed markedly reduced 3-nitrotyrosine (3-NT, $ONOO^-$ biomarker) levels compared to HCA and HPC. This attenuated the MMPs/TGF-β/EMT cascade, evidenced by E-cadherin upregulation and vimentin downregulation in HCAT (+) tumors. Collectively, the superior cytotoxic efficacy of HCAT (+) against residual tumor cells ultimately synergized with these mechanisms—vascular normalization alleviating hypoxia, $ONOO^-$ scavenging inhibiting immunosuppressive microenvironment, and EMT reversal suppressing invasive phenotypes— preventing distant pulmonary metastasis.

To visually track metastatic inhibition, 4T1-Luc cells pre-treated with therapeutic formulations for 24 h were administered *via* tail vein injection. Bioluminescent imaging was used to monitor tumor volume every 3 days, and mice were sacrificed at week 3 for imaging of lung metastasis foci (Fig. 12a). As shown in Fig. 12b, mice in the HPC (+) group and the control group exhibited pulmonary metastasis signals by day 3, progressing to widespread dissemination by day 9. Mortality commenced at day 15 (controls) and day 21 (HPC (+)), with histopathology confirming extensive lung metastases causing respiratory failure. This indicates that although HPC (+) slightly prolonged survival, it did not reduce metastasis risk. In contrast, nanoparticle-treated groups showed delayed metastasis onset, with no detectable signals until day 18 in HAT/HCT/HCA groups. Crucially, HCAT (+) mice remained metastasis-free throughout the 21-day study, corroborated by *ex vivo* imaging (Fig. 12c). This profound protection stemmed from HCAT's multimodal action: 1) Enhanced cytotoxicity significantly reduced viable tumor cells pre-injection; 2) Potent immunogenic cell death amplified systemic tumor clearance; 3) $ONOO^-$ scavenging (*via* TPE-4NMB) suppressed MMP/TGF-β-mediated EMT – a critical metastasis driver.

These findings confirmed that synergizing PDT-enhanced immunity with EMT cascade blockade provides a robust strategy to inhibit circulating tumor cell implantation and distant metastasis.

3.15. Capacity in inhibiting tumor recurrence

Given that the HCAT exhibited remarkable efficacy in enhancing the immunotherapeutic response against primary breast cancer in murine models, its potential to prevent tumor recurrence was assessed using a

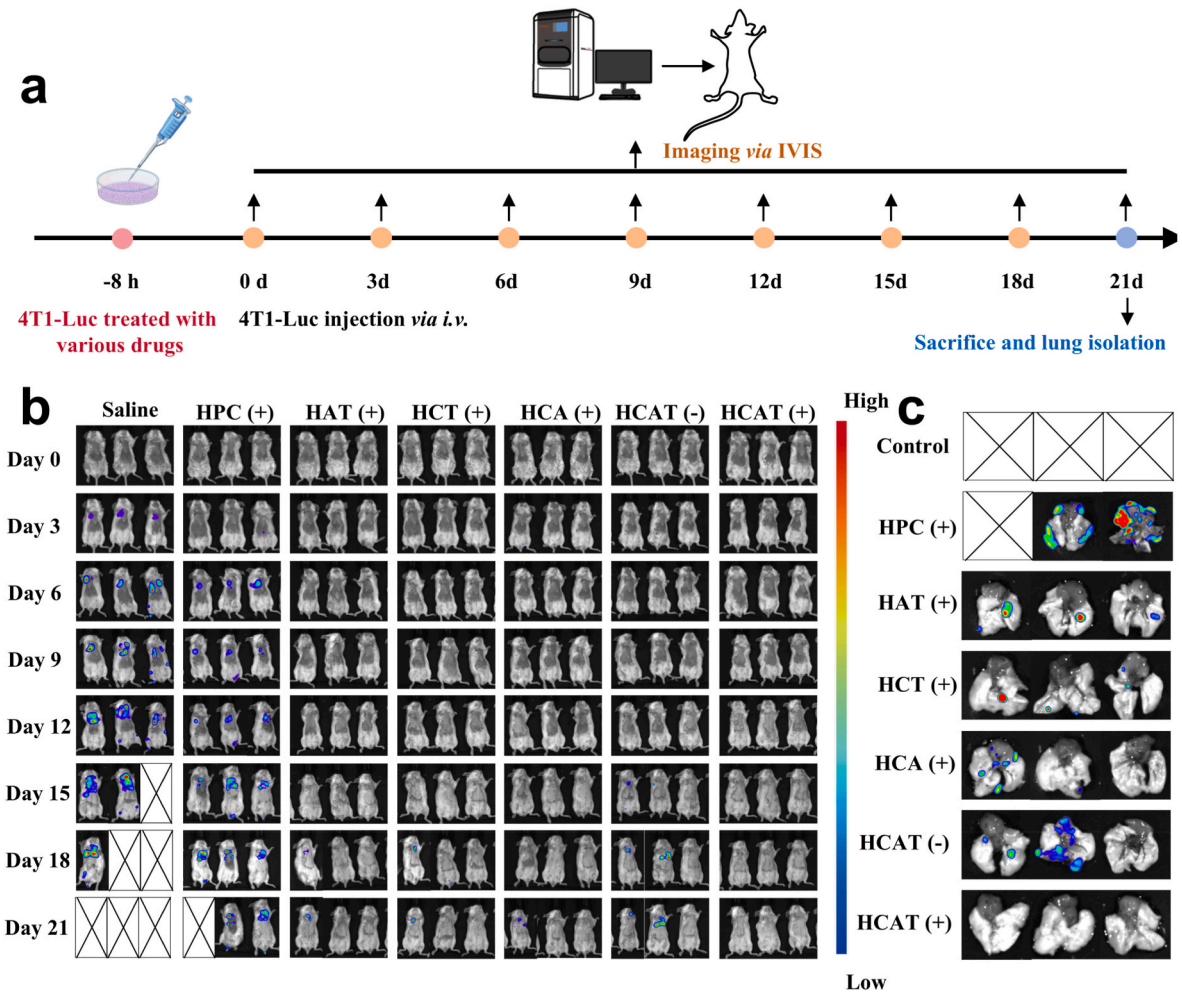

Fig. 12. Capacity of inhibiting distant metastasis of circulating tumor cells. a) Schematic illustration of the 4T1-Luc colonization model. b) *In vivo* bioluminescence imaging of BALB/c mice after tail vein injection of 4T1-luc pre-treated with different formulations (20 μg mL^{-1} as HPC) for various times (n = 3). c) *Ex vivo* bioluminescence images of lungs after tail vein injection of 4T1-luc cells pre-treated with different formulations for 21 days. The cross in the picture represents the corresponding mouse death.

4T1-luc resection-rechallenge model. As illustrated in Fig. 13a, the mice received three doses of treatment prior to the surgical excision of the left primary tumors. Bioluminescence intensity, which serves as an indicator of tumor volume, was monitored throughout the therapeutic regimen. On day 7, bioluminescence imaging revealed that the HCAT (+) group demonstrated the highest antitumor efficacy. By day 14, following surgical removal of the tumors, minimal residual tumor presence was noted in the left mammary gland. Subsequent rechallenge with 4T1-luc tumor cells in the right mammary gland allowed for the assessment of recurrent tumor volume. As depicted in Fig. 13b and c, both saline and HPC treatments failed to prevent tumor recurrence, as evidenced by an increase in recurrent tumor volume and lung metastasis by day 28. In contrast, the HCAT (+) treatment significantly inhibited tumor recurrence, with the tumor growth curves for this group exhibiting markedly slower progression compared to all other treatment groups.

Flow cytometry analysis elucidated the underlying mechanism responsible for the suppression of recurrence (Fig. 13d-h). The HCAT (+) group exhibited significantly increased proportions of mature DCs and $CD8^+$ T cells, along with decreased counts of Tregs and myeloid-derived suppressor cells (MDSCs) in tumors. These observations confirm that HCAT NPs effectively activate and sustain antitumor immune responses. In contrast, the other group demonstrated inadequate $CD8^+$ T cell infiltration and elevated levels of Tregs and MDSCs compared to the HCAT (+) group, which correlates with its inability to prevent distant metastasis.

As the largest immune organ in the body, the spleen can rapidly differentiate into effector T cells upon tumor antigen stimulation, thereby exerting anti-tumor immune responses. Changes in its immune cell subpopulations can reflect long-term systemic immune status. Hence, we analyzed immune cell profiles in spleens from each treatment group (Figure S18a-S18f). The results demonstrated that similar to the infiltration patterns observed in tumor tissues, the HCAT (+) group exhibited significantly elevated proportions of DCs and effector T cells in the spleen compared to other groups, reaching approximately 2.5-fold and 6-fold higher than the control group, respectively. Notably, the M1/M2 macrophage ratio was nearly 20-fold higher than the control. Conversely, immunosuppressive cell populations including Tregs and MDSCs showed 4-fold and 6-fold reductions compared to the control group.

Collectively, these findings indicate that HCAT nanoparticles induce durable antitumor immune memory by promoting DCs maturation, $CD8^+$ T cell activation, and reversing the immunosuppressive microenvironment, thereby effectively inhibiting tumor recurrence and metastasis.

3.16. Safety evaluation

Potential *in vivo* toxicity must be considered in the development of

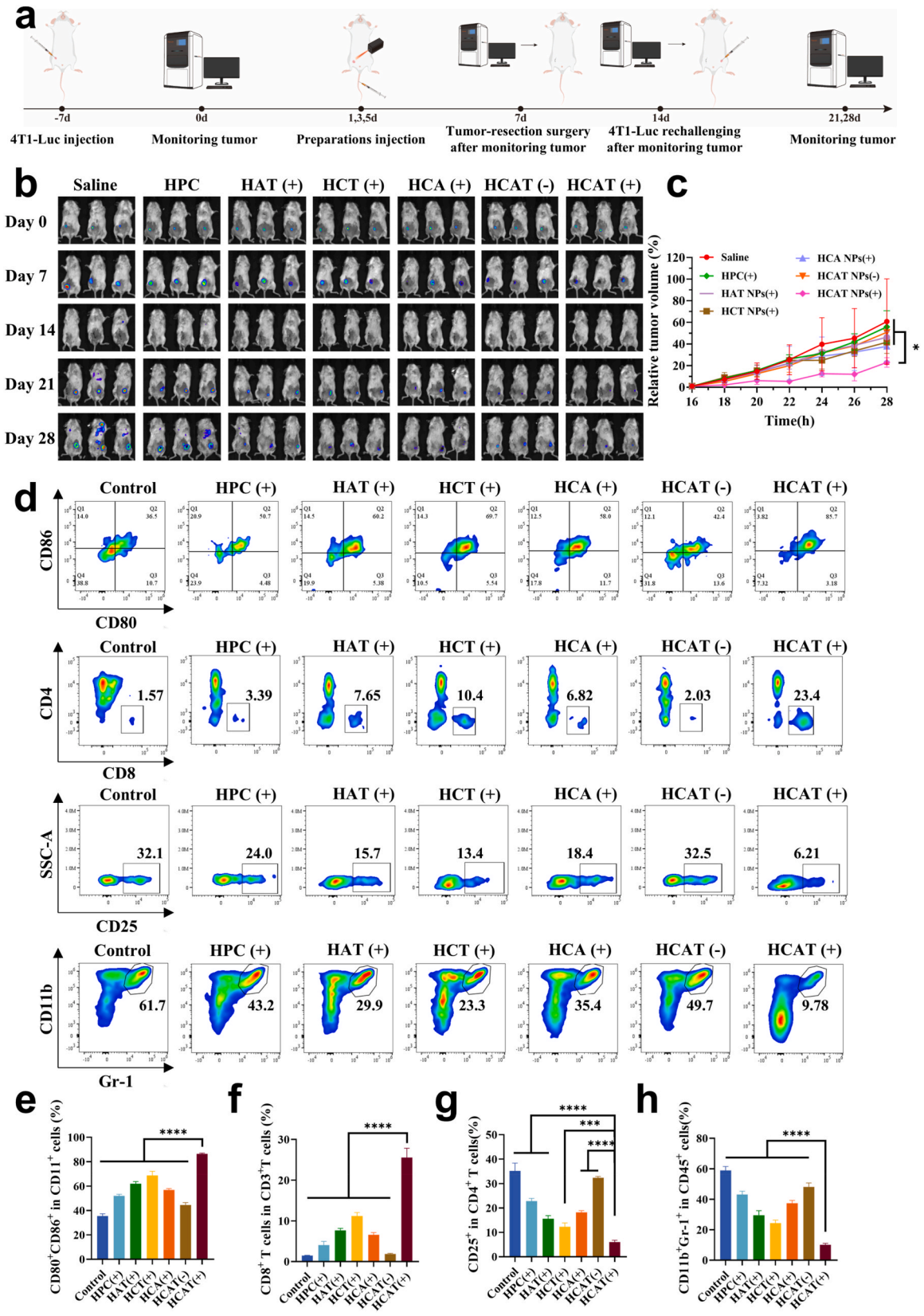

Fig. 13. Evaluation of long-term immune memory in the 4T1 recurrent model. a) Treatment timeline for recurrence efficacy test. b) Bioluminescence imaging of BALB/c mice with 4T1-Luc tumors post-treatment (2 mg kg^{-1} as HPC). c) Recurrent tumor growth curves post-surgery. d) Flow cytometry and e) quantitative analysis of mature DCs, f) $CD8^+$ T cells, g) Tregs, h) MDSCs, in the recurrent tumors. All the statistical data are presented as mean ± SD (n = 5). Statistical significance of c) was analyzed using two-way ANOVA. Statistical significance of e), f), g), and h) was analyzed using one-way ANOVA. *$p < 0.05$, ***$p < 0.001$, ****$p < 0.0001$.

novel nano-systems. The results showed that compared to the saline group, HCAT did not cause significant changes in mouse weight (Fig. S19a), blood biochemistry (Fig. S19b), organ index (Fig. S19c), *etc*., indicating that HCAT at the current dosage hardly causes side effects. Interestingly, HCAT could avoid the hemolysis risk caused by HPC *via* inhibiting the interaction between HPC-related groups and red blood cells (Fig. S19d), while H&E staining results showed that HCAT did not cause significant organ damage, such as necrosis or inflammation (Fig. S19e). All of these results indicate that HCAT possessed high biosafety and presented rare side effects to the mice.

4. Conclusions

In this study, we have reported an intelligent design of a laser-triggered cascade reaction-driven NO theranostic nanomotor with self-amplifying necrosis targeting and deep tumor penetration for enhanced type I photodynamic immunotherapy. The prepared HCAT NPs can accumulate to the tumor site *via* targeting necrotic tissues, while the recovered fluorescence emitted from HPC can be used to self-monitor the drug distribution and guide laser moment. Cu^{2+} has remarkably enhanced the type I photosensitivity of HPC *via* facilitating electron transfer and GSH depletion, while the cascade reaction triggered by the type I PDT has induced the generation of NO, which can synergetic promote the deep tumor penetration with HPC by enhancing the motion of nanomotor, and remodel the vascular network. Notably, the activated fluorescence emitted from TPE-4NM can be utilized to self-report the generation of NO, while TPE-4NMB can eliminate $ONOO^-$ which is related to tumor metastasis simultaneously. The well-designed HCAT NPs showed a noticeable antitumor immunotherapy effect on primary breast tumors, recurrent tumors, and distant metastasis. The nanomotor - HCAT NPs have provided an insightful idea and meaningful practice for the development of type I PSs and offer a novel strategy for cascade reaction-driven precision diagnostics and therapeutics in breast cancer.

CRediT authorship contribution statement

Yuanyuan Yu: Writing – original draft, Visualization, Project administration, Investigation. **Shuhui Chen:** Writing – original draft, Project administration. **Bin Zhao:** Methodology. **Lili Zhao:** Methodology, Formal analysis. **Fang Wang:** Project administration, Investigation. **Jingwei Xue:** Funding acquisition. **Zhongtao Zhang:** Writing – review & editing, Writing – original draft, Validation, Funding acquisition, Conceptualization.

Declaration of competing interest

The authors declare that they have no known competing financial interests or personal relationships that could have appeared to influence the work reported in this paper.

Acknowledgements

This work was financially supported by the National Natural Science Foundation of China (82202451, 82472139), Shandong Provincial Natural Science Foundation (ZR2024QH062), Postdoctoral Innovation Program of Shandong Province (SDCX-ZG-202301012), Taian Science and Technology Innovation Development Project (2023NS399), and National Key Research and Development Projects Intergovernmental Cooperation in Science and Technology of China (2023YFE0109800), Shandong Province Medical and Health Technology Project (202313021398).

Appendix A. Supplementary data

Supplementary data to this article can be found online at https://doi.org/10.1016/j.mtbio.2025.102677.

Data availability

Data will be made available on request.

References

[1] X. Li, J.F. Lovell, J. Yoon, X. Chen, Clinical development and potential of photothermal and photodynamic therapies for cancer, Nat. Rev. Clin. Oncol. 17 (11) (2020) 657–674, https://doi.org/10.1038/s41571-020-0410-2.
[2] J. Xie, Y. Wang, W. Choi, P. Jangili, Y. Ge, Y. Xu, J. Kang, L. Liu, B. Zhang, Z. Xie, J. He, N. Xie, G. Nie, H. Zhang, J.S. Kim, Overcoming barriers in photodynamic therapy harnessing nano-formulation strategies, Chem. Soc. Rev. 50 (16) (2021) 9152–9201, https://doi.org/10.1039/d0cs01370f.
[3] B. Ji, M. Wei, B. Yang, Recent advances in nanomedicines for photodynamic therapy (PDT)-driven cancer immunotherapy, Theranostics 12 (1) (2022) 434–458, https://doi.org/10.7150/thno.67300.
[4] M. Zhang, Y. Zhao, H. Ma, Y. Sun, J. Cao, How to improve photodynamic therapy-induced antitumor immunity for cancer treatment? Theranostics 12 (10) (2022) 4629–4655, https://doi.org/10.7150/thno.72465.
[5] M. Zhao, Y. Zhang, J. Miao, H. Zhou, Y. Jiang, Y. Zhang, M. Miao, W. Chen, W. Xing, Q. Li, Q. Miao, An activatable phototheranostic probe for anti-hypoxic type I Photodynamic- and immuno-therapy of cancer, Adv. Mater. 36 (4) (2024) e2305243, https://doi.org/10.1002/adma.202305243.
[6] R. Zheng, L. Zhao, C. Huang, H. Cheng, N. Yang, Z. Chen, H. Cai, W. Zhang, R. Kong, S. Li, Paraptosis inducer to effectively trigger immunogenic cell death for metastatic tumor immunotherapy with IDO inhibition, ACS Nano 17 (11) (2023) 9972–9986, https://doi.org/10.1021/acsnano.2c11964.
[7] Y. Zhong, Z. Qiu, K. Zhang, Z. Lu, Z. Li, Y. Cen, S. Li, H. Cheng, Plasma membrane targeted photodynamic nanoagonist to potentiate immune checkpoint blockade therapy by initiating tumor cell pyroptosis and depleting infiltrating B cells, Adv Mater 37 (13) (2025) e2415078, https://doi.org/10.1002/adma.202415078.
[8] Q. Zhou, G. Huang, J. Si, Y. Wu, S. Jin, Y. Ji, Z. Ge, Potent covalent organic framework nanophotosensitizers with staggered type I/II motifs for photodynamic immunotherapy of hypoxic tumors, ACS Nano 18 (52) (2024) 35671–35683, https://doi.org/10.1021/acsnano.4c14555.
[9] M.M. Wan, H. Chen, Z. Da Wang, Z.Y. Liu, Y.Q. Yu, L. Li, Z.Y. Miao, X.W. Wang, Q. Wang, C. Mao, J. Shen, J. Wei, Nitric oxide-driven nanomotor for deep tissue penetration and multidrug resistance reversal in cancer therapy, Adv. Sci. 8 (3) (2021) 2002525, https://doi.org/10.1002/advs.202002525.
[10] C. Yang, G. Mu, Y. Zhang, Y. Gao, W. Zhang, J. Liu, W. Zhang, P. Li, L. Yang, Z. Yang, J. Gao, J. Liu, Supramolecular nitric oxide depot for hypoxic tumor vessel normalization and radiosensitization, Adv. Mater. 34 (37) (2022) e2202625, https://doi.org/10.1002/adma.202202625.
[11] C.H. Richards, Z. Mohammed, T. Qayyum, P.G. Horgan, D.C. McMillan, The prognostic value of histological tumor necrosis in solid organ malignant disease: a systematic review, Future Oncol. 7 (10) (2011) 1223–1235, https://doi.org/10.2217/fon.11.99.
[12] R. Caruso, A. Parisi, A. Bonanno, D. Paparo, E. Quattrocchi, G. Branca, M. Scardigno, F. Fedele, Histologic coagulative tumour necrosis as a prognostic indicator of aggressiveness in renal, lung, thyroid and colorectal carcinomas: a brief review, Oncol. Lett. 3 (1) (2012) 16–18, https://doi.org/10.3892/ol.2011.420.
[13] J.M. Adrover, X. Han, L. Sun, T. Fujii, N. Sivetz, J. Dassler-Plenker, C. Evans, J. Peters, X. He, C.D. Cannon, W.J. Ho, G. Raptis, R.S. Powers, M. Egeblad, Neutrophils drive vascular occlusion, tumour necrosis and metastasis, Nature 645 (8080) (2025) 484–495, https://doi.org/10.1038/s41586-025-09278-3.
[14] M. Yang, L. Zhou, Y.Y. Zhao, K.M.K. Swamy, A. Chen, J. Yoon, The revolution of type I organic photosensitizers: current strategies and future directions, Science Bulletin 70 (8) (2025) 1203–1206, https://doi.org/10.1016/j.scib.2025.02.037.
[15] M. Li, J. Xiong, Y. Zhang, L. Yu, L. Yue, C. Yoon, Y. Kim, Y. Zhou, X. Chen, Y. Xu, X. Peng, J.S. Kim, New guidelines and definitions for type I photodynamic therapy, Chem. Soc. Rev. 54 (15) (2025) 7025–7057, https://doi.org/10.1039/d1cs01079d.
[16] D. Cai, J.M. Mataraza, Z. Qin, Z. Huang, J. Huang, T.C. Chiles, D. Carnahan, K. Kempa, Z. Ren, Highly efficient molecular delivery into mammalian cells using carbon nanotube spearing, Nat. Methods 2 (6) (2005) 449–454, https://doi.org/10.1038/nmeth761.
[17] H. Chen, T. Shi, Y. Wang, Z. Liu, F. Liu, H. Zhang, X. Wang, Z. Miao, B. Liu, M. Wan, C. Mao, J. Wei, Deep penetration of nanolevel drugs and micrometer-level T cells promoted by nanomotors for cancer immunochemotherapy, J. Am. Chem. Soc. 143 (31) (2021) 12025–12037, https://doi.org/10.1021/jacs.1c03071.
[18] M. Tang, J. Ni, Z. Yue, T. Sun, C. Chen, X. Ma, L. Wang, Polyoxometalate-Nanozyme-Integrated nanomotors (POMotors) for self-propulsion-promoted synergistic photothermal-catalytic tumor therapy, Angew Chem. Int. Ed. Engl. 63 (6) (2024) e202315031, https://doi.org/10.1002/anie.202315031.
[19] A. Escudero, F.J. Hicke, E. Lucena-Sánchez, S. Pradana-López, J.J. Esteve-Moreno, V. Sanz-Álvarez, I. Garrido-Cano, S. Torres-Ruiz, J.M. Cejalvo, A. García-Fernández, P. Díez, R. Martinez-Manez, Glucose-Fueled gated nanomotors: enhancing in vivo anticancer efficacy via deep drug penetration into tumors, ACS Nano 19 (22) (2025) 20932–20955, https://doi.org/10.1021/acsnano.5c03799.
[20] H. Choi, S. Jeong, C. Simó, A. Bakenecker, J. Liop, H.S. Lee, T.Y. Kim, C. Kwak, G. Y. Koh, S. Sánchez, S.K. Hahn, Urease-powered nanomotor containing STING

agonist for bladder cancer immunotherapy, Nat. Commun. 15 (1) (2024) 9916–9934, https://doi.org/10.1038/s41467-024-54293-z.
[21] H. Tan, Z. Hu, J. Miao, B. Chen, H. Li, J. Gao, Y. Ye, W. Xu, J. Jiang, H. Qin, Enzymatic nanomotors with chemotaxis for product-based cancer therapy, J. Contr. Release (2025) 377, https://doi.org/10.1016/j.jconrel.2024.11.042.
[22] J. Wang, J. Liu, Y. Sümbelli, J. Shao, X. Shi, J.C.M. van Hest, Nanogel-based nitric oxide-driven nanomotor for deep tissue penetration and enhanced tumor therapy, J. Contr. Release 372 (2024) 59–68, https://doi.org/10.1016/j.jconrel.2024.06.021.
[23] Z. Hu, H. Tan, Y. Ye, W. Xu, J. Gao, L. Liu, L. Zhang, J. Jiang, H. Tian, F. Peng, Y. Tu, NIR-Actuated ferroptosis nanomotor for enhanced tumor penetration and therapy, Adv. Mater. 36 (49) (2024) e2412227, https://doi.org/10.1002/adma.202412227.
[24] Y. Li, Y. Li, G. He, X. Li, R. Ding, R. Yan, J. Lin, P. Huang, Activatable enzymatic nanoplatform incorporated into microneedle patch for relieving tumor Hypoxia augmented photodynamic therapy, Adv. Mater. (2025) e2504258, https://doi.org/10.1002/adma.202504258.
[25] Z. Zhang, R. Wang, R. Luo, J. Zhu, X. Huang, W. Liu, F. Liu, F. Feng, W. Qu, An activatable theranostic nanoprobe for dual-modal imaging-guided photodynamic therapy with self-reporting of sensitizer activation and therapeutic effect, ACS Nano 15 (3) (2021) 5366–5383, https://doi.org/10.1021/acsnano.0c10916.
[26] J. Zhuang, S. Liu, B. Li, Z. Li, C. Wu, D. Xu, W. Pan, Z. Li, X. Liu, B. Liu, Electron transfer mediator modulates type II porphyrin-based metal-organic framework photosensitizers for type I photodynamic therapy, Angew Chem. Int. Ed. Engl. 64 (9) (2025) e202420643, https://doi.org/10.1002/anie.202420643.
[27] M. Qiu, D. Wang, H. Huang, T. Yin, W. Bao, B. Zhang, Z. Xie, N. Xie, Z. Wu, C. Ge, Q. Wang, M. Gu, H.L. Kutscher, L. Liu, S. Bao, P.N. Prasad, H. Zhang, A regioselectively oxidized 2D Bi/BiOx lateral nano-heterostructure for hypoxic photodynamic therapy, Adv. Mater. 33 (49) (2021) e2102562, https://doi.org/10.1002/adma.202102562.
[28] Q. Xin, H. Shah, A. Nawaz, W. Xie, M.Z. Akram, A. Batool, L. Tian, S.U. Jan, R. Boddula, B. Guo, Q. Liu, J.R. Gong, Antibacterial carbon-based nanomaterials, Adv. Mater. 31 (45) (2019) e1804838, https://doi.org/10.1002/adma.201804838.
[29] W. Chen, Y. Zhang, H. Yi, F. Wang, X. Chu, J. Jiang, Type I photosensitizer targeting G-Quadruplex RNA elicits augmented immunity for cancer ablation, Angew Chem. Int. Ed. Engl. 62 (17) (2023) e202300162, https://doi.org/10.1002/anie.202300162.
[30] Q. Zhan, Y. Kuang, X. Chen, Y. Yang, L. Jiang, J. Chen, L. Li, J. Wang, S. Zhu, H. Huang, L. Wang, P. Zhu, R. Liu, Photo-generating Type-I ROS and aryl radicals by mitochondrial-targeting oxime-ester photogenerator for pyroptosis-mediated anti-hypoxia photoimmunotherapy, Bioact. Mater. 47 (2025) 327–342, https://doi.org/10.1016/j.bioactmat.2025.01.032.
[31] Y. Yu, S. Wu, L. Zhang, S. Xu, C. Dai, S. Gan, G. Xie, G. Feng, B.Z. Tang, Cationization to boost both type I and type II ROS generation for photodynamic therapy, Biomaterials 280 (2022) 121255, https://doi.org/10.1016/j.biomaterials.2021.121255.
[32] Y. Zhu, F. Wu, B. Zheng, Y. Yang, J. Yang, H. Xiong, Electron-Withdrawing substituents enhance the type I PDT and NIR-II fluorescence of BODIPY J aggregates for bioimaging and cancer therapy, Nano Lett. 24 (27) (2024) 8287–8295, https://doi.org/10.1021/acs.nanolett.4c01339.
[33] J. Zhuang, G. Qi, Y. Feng, M. Wu, H. Zhang, D. Wang, X. Zhang, K.C. Chong, B. Li, S. Liu, J. Tian, Y. Shan, D. Mao, B. Liu, Thymoquinone as an electron transfer mediator to convert Type II photosensitizers to Type I photosensitizers, Nat. Commun. 15 (1) (2024) 4943, https://doi.org/10.1038/s41467-024-49311-z.
[34] T. Xu, Q. Ma, C. Zhang, X. He, Q. Wang, Y. Wu, K. Qin, F. Liao, P. Zhou, P. Xu, J. Yang, J. Yang, J. Chang, L. Qiao, Y. Hu, A novel nanomedicine for osteosarcoma treatment: triggering ferroptosis through GSH depletion and inhibition for enhanced synergistic PDT/PTT therapy, J. Nanobiotechnol. 23 (2025) 323, https://doi.org/10.1186/s12951-025-03380-4.
[35] W. Zhang, J. Lu, X. Gao, P. Li, W. Zhang, Y. Ma, H. Wang, B. Tang, Enhanced photodynamic therapy by reduced levels of intracellular glutathione obtained by employing a Nano-MOF with Cu (II) as the active Center, Angew Chem. Int. Ed. Engl. 57 (18) (2018) 4891–4896, https://doi.org/10.1002/anie.201710800.
[36] S. Wang, N. Xu, S. Yu, W. Si, M. Yang, Y. Liu, Y. Zheng, S. Zhao, J. Shi, J. Yuan, Hyaluronic acid-coated porphyrin nanoplatform with oxygen sustained supplying and glutathione depletion for enhancing photodynamic/ion/chemo synergistic cancer treatment, Int. J. Biol. Macromol. 278 (2024) 134661, https://doi.org/10.1016/j.ijbiomac.2024.134661.
[37] H. Liang, Z. Zhou, R. Luo, M. Sang, B. Liu, M. Sun, W. Qu, F. Feng, W. Liu, Tumor-specific activated photodynamic therapy with an oxidation-regulated strategy for enhancing anti-tumor efficacy, Theranostics 8 (18) (2018) 5059–5071, https://doi.org/10.7150/thno.28344.
[38] Z. Zhang, R. Wang, X. Huang, R. Luo, J. Xue, J. Gao, W. Liu, F. Liu, F. Feng, W. Qu, Self-Delivered and self-monitored chemo-photodynamic nanoparticles with light-triggered synergistic antitumor therapies by downregulation of HIF-1α and depletion of GSH, ACS Appl. Mater. Interfaces 12 (5) (2020) 5680–5694, https://doi.org/10.1021/acsami.9b23325.
[39] Z. Zhang, Y. Yu, S. Liu, J. Li, B. Zhao, F. Wang, Z. Zhao, Q. Ni, F. Liu, J. Xue, Simultaneous visualization and depletion of peroxynitrite by a simple aggregation-induced emission nanoprobe for preventing breast cancer metastasis after surgery, Anal. Chem. 96 (10) (2024) 4180–4189, https://doi.org/10.1021/acs.analchem.3c05292.
[40] Y. Guo, J. Wang, G. Li, Z. Wang, Y. Li, S. Sun, J.C.M. van Hest, M. Shen, X. Shi, Oxygen and heat Dual-Driven Stomatocyte nanomotors for highly efficient inflammation-relieved breast tumor photothermal therapy, Adv. Funct. Mater. (2025) 2500113, https://doi.org/10.1002/adfm.202500113.
[41] X. Guo, W. Luo, L. Wu, L. Zhang, Y. Chen, T. Li, H. Li, W. Zhang, Y. Liu, J. Zheng, Y. Wang, Natural products from herbal medicine self-assemble into advanced bioactive materials, Adv. Sci. 11 (35) (2024) e2403388, https://doi.org/10.1002/advs.202403388.
[42] Y.L. Wang, Y. Mu, Y.L. Zhang, X. Luo, T. Peng, Y. Tan, X. Wang, L. Feng, J. Chen, Q. Hua, Accessible and effective nanomedicines: self-assembly products from Chinese herbal medicines (CHMs), Adv. Funct. Mater. 35 (9) (2025) e2416151, https://doi.org/10.1002/adfm.202416151.
[43] Z. Zhang, K. Zhang, R. Wang, J. Zhu, J. Xue, F. Liu, H. Chi, H. Yang, F. Feng, W. Liu, W. Qu, A self-amplified necrotic targeting theranostic nanoparticle with deep tumor penetration for imaging-guided personalized chemo-photodynamic therapy, Chem. Eng. J. 455 (2023) 140465, https://doi.org/10.1016/j.cej.2022.140465.
[44] C.L.L. Saw, M. Olivo, K.C. Soo, P.W.S. Heng, Delivery of hypericin for photodynamic applications, Cancer Lett. 241 (1) (2006) 23–30, https://doi.org/10.1016/j.canlet.2005.10.020.
[45] L. Wu, W. Pi, X. Huang, L. Yang, X. Zhang, J. Lu, S. Yao, X. Lin, X. Tan, Z. Wang, P. Wang, Orchestrated metal-coordinated carrier-free celastrol hydrogel intensifies T cell activation and regulates response to immune checkpoint blockade for synergistic chemo-immunotherapy, Biomaterials 312 (2025) 122723, https://doi.org/10.1016/j.biomaterials.2024.122723.
[46] F. Fang, S. Wang, Y. Song, M. Sun, W. Chen, D. Zhao, J. Zhang, Continuous spatiotemporal therapy of a Full-API nanodrug via multi-step tandem endogenous biosynthesis, Nat. Commun. 14 (1) (2023) 1660, https://doi.org/10.1038/s41467-023-37315-0.
[47] E.N. Tcyganov, E. Sanseviero, D. Marvel, T. Beer, H.Y. Tang, P. Hembach, D. W. Speicher, Q. Zhang, L.R. Donthireddy, A. Mostafa, S. Tsyganova, V. Pisarev, T. Laufer, D. Ignatov, S. Ferrone, C. Meyer, H.H. Maby-El, D.E. Speiser, S. Altiok, S. Antonia, X. Xu, W. Xu, C. Zheng, L.M. Schuchter, R.K. Amaravadi, T.C. Mitchell, G.C. Karakousis, Z. Yuan, L.J. Montaner, E. Celis, D.I. Gabrilovich, Peroxynitrite in the tumor microenvironment changes the profile of antigens allowing escape from cancer immunotherapy, Cancer Cell 40 (10) (2022) 1173–1189.e6, https://doi.org/10.1016/j.ccell.2022.09.001.
[48] T. Okamoto, T. Akaike, T. Sawa, Y. Miyamoto, A. van der Vliet, H. Maeda, Activation of matrix metalloproteinases by peroxynitrite-induced protein S-glutathiolation via disulfide S-oxide formation, J. Biol. Chem. 276 (31) (2001) 29596–29602, https://doi.org/10.1074/jbc.M102417200.
[49] P. Pacher, J.S. Beckman, L. Liaudet, Nitric oxide and peroxynitrite in health and disease, Physiol. Rev. 87 (1) (2007) 315–424, https://doi.org/10.1152/physrev.00029.2006.
[50] X. Han, O. Taratula, O. Taratula, K. Xu, A. St Lorenz, A. Moses, Y. Jahangiri, G. Yu, K. Farsad, Biodegradable hypericin-containing nanoparticles for necrosis targeting and fluorescence imaging, Mol. Pharm. 17 (5) (2020) 1538–1545, https://doi.org/10.1021/acs.molpharmaceut.9b01238.
[51] J. Xiang, M. Suo, J. Lan, et al., Novel carrier-free nanomedicine for regulating macrophage phenotype to amplify anti-tumor photoimmunotherapy, Small (2025) e05304.
[52] Y. Sung, P. Jin, L. Chu, F. Hsu, M. Wang, C. Chang, S. Chiou, J. Qiu, D. Gao, C. Lin, Y. Chen, Y. Hsu, J. Wang, F. Wang, P. Yu, A. Chiang, A. Wu, J. Ko, C. Lai, T. Lu, Y. Chen, Delivery of nitric oxide with a nanocarrier promotes tumour vessel normalization and potentiates anti-cancer therapies, Nat. Nanotechnol. 14 (12) (2019) 1160–1169, https://doi.org/10.1038/s41565-019-0570-3.